DESY 13-058 ISSN 0418-9833
April 2013

Elastic and Proton-Dissociative Photoproduction of J/ψ Mesons at HERA

H1 Collaboration

Abstract

Cross sections for elastic and proton-dissociative photoproduction of J/ψ mesons are measured with the H1 detector in positron-proton collisions at HERA. The data were collected at ep centre-of-mass energies $\sqrt{s} \approx 318$ GeV and $\sqrt{s} \approx 225$ GeV, corresponding to integrated luminosities of $\mathcal{L} = 130\,\mathrm{pb}^{-1}$ and $\mathcal{L} = 10.8\,\mathrm{pb}^{-1}$, respectively. The cross sections are measured as a function of the photon-proton centre-of-mass energy in the range $25 < W_{\gamma p} < 110$ GeV. Differential cross sections $\mathrm{d}\sigma/\mathrm{d}t$, where t is the squared four-momentum transfer at the proton vertex, are measured in the range $|t| < 1.2$ GeV^2 for the elastic process and $|t| < 8$ GeV^2 for proton dissociation. The results are compared to other measurements. The $W_{\gamma p}$ and t-dependences are parametrised using phenomenological fits.

Submitted to *Eur. Phys. J.* **C**

C. Alexa[5], V. Andreev[25], A. Baghdasaryan[37], S. Baghdasaryan[37], W. Bartel[11], K. Begzsuren[34], A. Belousov[25], P. Belov[11], V. Boudry[28], I. Bozovic-Jelisavcic[2], G. Brandt[49], M. Brinkmann[11], V. Brisson[27], D. Britzger[11], A. Buniatyan[14], A. Bylinkin[24,46], L. Bystritskaya[24], A.J. Campbell[11], K.B. Cantun Avila[22], F. Ceccopieri[4], K. Cerny[31], V. Chekelian[26], J.G. Contreras[22], J. Cvach[30], J.B. Dainton[18], K. Daum[36,41], E.A. De Wolf[4], C. Diaconu[21], M. Dobre[5], V. Dodonov[13], A. Dossanov[12,26], G. Eckerlin[11], S. Egli[35], E. Elsen[11], L. Favart[4], A. Fedotov[24], R. Felst[11], J. Feltesse[10], J. Ferencei[16], D.-J. Fischer[11], M. Fleischer[11], A. Fomenko[25], E. Gabathuler[18], J. Gayler[11], S. Ghazaryan[11], A. Glazov[11], L. Goerlich[7], N. Gogitidze[25], M. Gouzevitch[11,42], C. Grab[39], A. Grebenyuk[11], T. Greenshaw[18], G. Grindhammer[26], S. Habib[11], D. Haidt[11], R.C.W. Henderson[17], E. Hennekemper[15], M. Herbst[15], G. Herrera[23], M. Hildebrandt[35], K.H. Hiller[38], J. Hladkỳ[30], D. Hoffmann[21], R. Horisberger[35], T. Hreus[4], F. Huber[14], M. Jacquet[27], X. Janssen[4], L. Jönsson[20], H. Jung[11,4], M. Kapichine[9], C. Kiesling[26], M. Klein[18], C. Kleinwort[11], R. Kogler[12], P. Kostka[38], M. Krämer[11], J. Kretzschmar[18], K. Krüger[11], M.P.J. Landon[19], W. Lange[38], P. Laycock[18], A. Lebedev[25], S. Levonian[11], K. Lipka[11,45], B. List[11], J. List[11], B. Lobodzinski[11], R. Lopez-Fernandez[23], V. Lubimov[24,†], E. Malinovski[25], H.-U. Martyn[1], S.J. Maxfield[18], A. Mehta[18], A.B. Meyer[11], H. Meyer[36], J. Meyer[11], S. Mikocki[7], I. Milcewicz-Mika[7], A. Morozov[9], J.V. Morris[6], K. Müller[40], Th. Naumann[38], P.R. Newman[3], C. Niebuhr[11], D. Nikitin[9], G. Nowak[7], K. Nowak[12], J.E. Olsson[11], D. Ozerov[11], P. Pahl[11], V. Palichik[9], M. Pandurovic[2], C. Pascaud[27], G.D. Patel[18], E. Perez[10,43], A. Petrukhin[11], I. Picuric[29], H. Pirumov[14], D. Pitzl[11], R. Plačakytė[11,45], B. Pokorny[31], R. Polifka[31,47], V. Radescu[11,45], N. Raicevic[29], T. Ravdandorj[34], P. Reimer[30], E. Rizvi[19], P. Robmann[40], R. Roosen[4], A. Rostovtsev[24], M. Rotaru[5], J.E. Ruiz Tabasco[22], S. Rusakov[25], D. Šálek[31], D.P.C. Sankey[6], M. Sauter[14], E. Sauvan[21,48], S. Schmitt[11], L. Schoeffel[10], A. Schöning[14], H.-C. Schultz-Coulon[15], F. Sefkow[11], S. Shushkevich[11], Y. Soloviev[11,25], P. Sopicki[7], D. South[11], V. Spaskov[9], A. Specka[28], Z. Staykova[4], M. Steder[11], B. Stella[32], G. Stoicea[5], U. Straumann[40], T. Sykora[4,31], P.D. Thompson[3], D. Traynor[19], P. Truöl[40], I. Tsakov[33], B. Tseepeldorj[34,44], J. Turnau[7], A. Valkárová[31], C. Vallée[21], P. Van Mechelen[4], Y. Vazdik[25], D. Wegener[8], E. Wünsch[11], J. Žáček[31], J. Zálešák[30], Z. Zhang[27], R. Žlebčík[31], H. Zohrabyan[37], and F. Zomer[27]

[1] *I. Physikalisches Institut der RWTH, Aachen, Germany*
[2] *Vinca Institute of Nuclear Sciences, University of Belgrade, 1100 Belgrade, Serbia*
[3] *School of Physics and Astronomy, University of Birmingham, Birmingham, UK*[b]
[4] *Inter-University Institute for High Energies ULB-VUB, Brussels and Universiteit Antwerpen, Antwerpen, Belgium*[c]
[5] *National Institute for Physics and Nuclear Engineering (NIPNE) , Bucharest, Romania*[k]
[6] *STFC, Rutherford Appleton Laboratory, Didcot, Oxfordshire, UK*[b]
[7] *Institute for Nuclear Physics, Cracow, Poland*[d]
[8] *Institut für Physik, TU Dortmund, Dortmund, Germany*[a]
[9] *Joint Institute for Nuclear Research, Dubna, Russia*
[10] *CEA, DSM/Irfu, CE-Saclay, Gif-sur-Yvette, France*
[11] *DESY, Hamburg, Germany*
[12] *Institut für Experimentalphysik, Universität Hamburg, Hamburg, Germany*[a]
[13] *Max-Planck-Institut für Kernphysik, Heidelberg, Germany*
[14] *Physikalisches Institut, Universität Heidelberg, Heidelberg, Germany*[a]

[15] *Kirchhoff-Institut für Physik, Universität Heidelberg, Heidelberg, Germany*[a]
[16] *Institute of Experimental Physics, Slovak Academy of Sciences, Košice, Slovak Republic*[e]
[17] *Department of Physics, University of Lancaster, Lancaster, UK*[b]
[18] *Department of Physics, University of Liverpool, Liverpool, UK*[b]
[19] *School of Physics and Astronomy, Queen Mary, University of London, London, UK*[b]
[20] *Physics Department, University of Lund, Lund, Sweden*[f]
[21] *CPPM, Aix-Marseille Univ, CNRS/IN2P3, 13288 Marseille, France*
[22] *Departamento de Fisica Aplicada, CINVESTAV, Mérida, Yucatán, México*[i]
[23] *Departamento de Fisica, CINVESTAV IPN, México City, México*[i]
[24] *Institute for Theoretical and Experimental Physics, Moscow, Russia*[j]
[25] *Lebedev Physical Institute, Moscow, Russia*
[26] *Max-Planck-Institut für Physik, München, Germany*
[27] *LAL, Université Paris-Sud, CNRS/IN2P3, Orsay, France*
[28] *LLR, Ecole Polytechnique, CNRS/IN2P3, Palaiseau, France*
[29] *Faculty of Science, University of Montenegro, Podgorica, Montenegro*[l]
[30] *Institute of Physics, Academy of Sciences of the Czech Republic, Praha, Czech Republic*[g]
[31] *Faculty of Mathematics and Physics, Charles University, Praha, Czech Republic*[g]
[32] *Dipartimento di Fisica Università di Roma Tre and INFN Roma 3, Roma, Italy*
[33] *Institute for Nuclear Research and Nuclear Energy, Sofia, Bulgaria*
[34] *Institute of Physics and Technology of the Mongolian Academy of Sciences, Ulaanbaatar, Mongolia*
[35] *Paul Scherrer Institut, Villigen, Switzerland*
[36] *Fachbereich C, Universität Wuppertal, Wuppertal, Germany*
[37] *Yerevan Physics Institute, Yerevan, Armenia*
[38] *DESY, Zeuthen, Germany*
[39] *Institut für Teilchenphysik, ETH, Zürich, Switzerland*[h]
[40] *Physik-Institut der Universität Zürich, Zürich, Switzerland*[h]

[41] *Also at Rechenzentrum, Universität Wuppertal, Wuppertal, Germany*
[42] *Also at IPNL, Université Claude Bernard Lyon 1, CNRS/IN2P3, Villeurbanne, France*
[43] *Also at CERN, Geneva, Switzerland*
[44] *Also at Ulaanbaatar University, Ulaanbaatar, Mongolia*
[45] *Supported by the Initiative and Networking Fund of the Helmholtz Association (HGF) under the contract VH-NG-401 and S0-072*
[46] *Also at Moscow Institute of Physics and Technology, Moscow, Russia*
[47] *Also at Department of Physics, University of Toronto, Toronto, Ontario, Canada M5S 1A7*
[48] *Also at LAPP, Université de Savoie, CNRS/IN2P3, Annecy-le-Vieux, France*
[49] *Department of Physics, Oxford University, Oxford, UK*[b]

† *Deceased*

[a] *Supported by the Bundesministerium für Bildung und Forschung, FRG, under contract numbers 05H09GUF, 05H09VHC, 05H09VHF, 05H16PEA*
[b] *Supported by the UK Science and Technology Facilities Council, and formerly by the UK Particle Physics and Astronomy Research Council*
[c] *Supported by FNRS-FWO-Vlaanderen, IISN-IIKW and IWT and by Interuniversity Attraction Poles Programme, Belgian Science Policy*

[d] *Partially Supported by Polish Ministry of Science and Higher Education, grant DPN/N168/DESY/2009*
[e] *Supported by VEGA SR grant no. 2/7062/ 27*
[f] *Supported by the Swedish Natural Science Research Council*
[g] *Supported by the Ministry of Education of the Czech Republic under the projects LC527, INGO-LA09042 and MSM0021620859*
[h] *Supported by the Swiss National Science Foundation*
[i] *Supported by CONACYT, México, grant 48778-F*
[j] *Russian Foundation for Basic Research (RFBR), grant no 1329.2008.2 and Rosatom*
[k] *Supported by the Romanian National Authority for Scientific Research under the contract PN 09370101*
[l] *Partially Supported by Ministry of Science of Montenegro, no. 05-1/3-3352*

1 Introduction

This paper reports a measurement of diffractive J/ψ photoproduction in positron-proton interactions at HERA, $ep \to e\ J/\psi\ X$. For the elastic regime X denotes a proton, whereas for the proton-dissociative regime X denotes a proton-dissociative system Y of mass $m_p < M_Y < 10\,\mathrm{GeV}$, as depicted in figures 1.

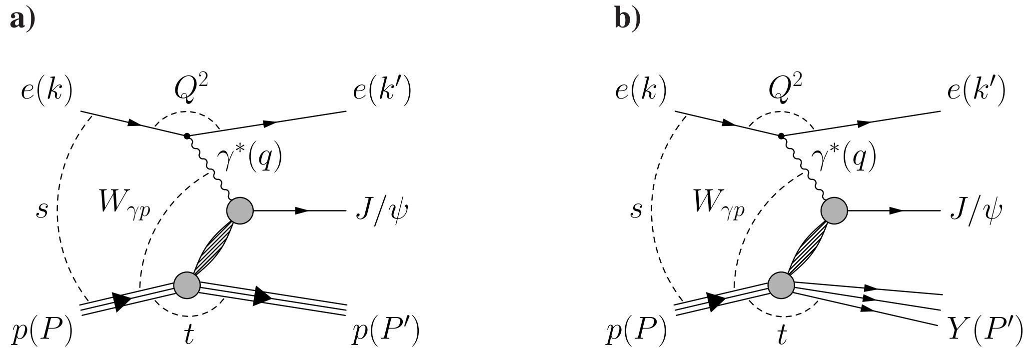

Figure 1: Diffractive J/ψ meson production in electron proton collisions: a) elastic J/ψ production in which the proton stays intact and b) proton-dissociative J/ψ production in which the proton dissociates to a low mass excited state with mass $M_Y > m_p$.

Diffractive vector meson production is characterised by the t-channel exchange of a colourless object between the incoming photon and proton. In the high-energy limit Regge theory predicts [1,2] an approximate cross section dependence $\sigma \propto W_{\gamma p}^{\delta}$ as a function of the photon-proton centre-of-mass energy $W_{\gamma p}$. For elastic production of light vector mesons (ρ, ω, ϕ) exponents $\delta \approx 0.22$ [3] are observed. In contrast, the cross section for elastic J/ψ production, $\gamma p \to J/\psi p$, rises more steeply with $W_{\gamma p}$, $\delta \approx 0.7$ [4,5], and is thus incompatible with a universal pomeron hypothesis [2]. The $W_{\gamma p}$ dependence of proton-dissociative J/ψ production [6–8] is expected to be similar to the elastic case.

Due to the presence of a hard scale, the mass of the J/ψ meson, calculations in perturbative Quantum-Chromo-Dynamics (QCD) are possible. The diffractive production of vector mesons can then be described in the proton rest frame by a process in which the photon fluctuates into a $q\bar{q}$ pair (or colour-dipole) at a long distance from the proton target. The $q\bar{q}$ pair interacts with the proton via a colour-singlet exchange, which in lowest order QCD is realised as a colourless gluon pair [9–12]. The steep rise of the cross section with $W_{\gamma p}$ is then related to the rise of the square of the gluon density towards low values of Bjorken x [13–17].

The elastic and proton-dissociative J/ψ cross sections as functions of the squared four-momentum transfer t at the proton vertex show a fast fall with increasing $|t|$ [4,5,18–25]. For the elastic J/ψ cross section the t-dependence can be parametrised by an exponential function $\mathrm{d}\sigma/\mathrm{d}t \propto e^{-b_{el}|t|}$ as expected from diffractive scattering. In an optical model the t-dependence of the elastic cross section carries information on the transverse size of the interaction region. The proton-dissociative cross section falls less steeply than the elastic one and becomes dominant at $|t| \gtrsim 1\,\mathrm{GeV}^2$. The differential proton-dissociative cross section as a function of t is parametrised with a power-law function $\mathrm{d}\sigma/\mathrm{d}t \propto (1 + (b_{pd}/n)|t|)^{-n}$, which for low $|t|$ has an approximate exponential behaviour, $\propto e^{-b_{pd}|t|}$.

Diffractive J/ψ production has been studied previously at HERA at low values of $|t|$ [4, 5, 18–23], and also at very large values of $|t|$ [24, 25], where proton-dissociative J/ψ production dominates.

In this analysis cross sections are determined simultaneously for the elastic and proton-dissociative regimes. In addition to a measurement at the nominal ep centre-of-mass energy of $\sqrt{s} \approx 318\,\mathrm{GeV}$, data recorded at a lower centre-of-mass energy of $\sqrt{s} \approx 225\,\mathrm{GeV}$ are analysed. This low-energy data set extends the kinematic region in $W_{\gamma p}$ into the transition region between previous diffractive J/ψ measurements at HERA and fixed target experiments [26,27]. The elastic and proton-dissociative cross sections as functions of t and $W_{\gamma p}$ are subjected to phenomenological fits, together with previous H1 data [4, 24], and are compared with QCD based dipole models [14].

2 Experimental Method

2.1 Kinematics

The kinematics of the processes $ep \to e\, J/\psi\, X$, where $X = p$ or Y (depicted in figure 1), are described by the following variables: the square of the ep centre-of-mass energy $s = (P + k)^2$, the square of the γp centre-of-mass energy $W^2_{\gamma p} = (q + k)^2$, the absolute value of the four-momentum transfer squared at the lepton vertex $Q^2 = -q^2 = -(k - k')^2$ and of the four-momentum transfer squared at the proton vertex $t = (P - P')^2$. The four-momenta k, k', P, P' and q refer to the incident and scattered beam positron, the incoming and outgoing proton (or dissociated system Y) and the exchanged photon, respectively.

In the limit of photoproduction, i.e $Q^2 \to 0$, the beam positron is scattered at small angles and escapes detection. In this regime the square of the γp centre-of-mass energy can be reconstructed via the variable $W^2_{\gamma p,rec} = s\, y^{rec}$, where y^{rec} is the reconstructed inelasticity, measured as $y^{rec} = \left(E_{J/\psi} - p_{z,\,J/\psi}\right) / \left(2\, E_e\right)$. Here, $E_{J/\psi}$ and $p_{z,\,J/\psi}$ denote the reconstructed energy and the momentum along the proton beam direction (z-axis) of the J/ψ meson and E_e is the positron beam energy. Furthermore, the variable t can be estimated from the transverse momentum of the J/ψ in the laboratory frame via the observable $t_{rec} = -p^2_{T,J/\psi}$. The reconstructed variables $W_{\gamma p,rec}$ and t_{rec} are only approximately equal to the variables $W_{\gamma p}$ and t, due to their definition and due to the smearing effects of the detector. In particular, $-p^2_{T,J/\psi}$ is systematically larger than t for events with a value of Q^2 close to the upper boundary of $2.5\,\mathrm{GeV}^2$ used in the analysis. In such events the J/ψ recoils against the scattered beam positron in addition to the proton. The measurement presented here corrects for this recoil effect by the unfolding procedure described below.

2.2 Monte Carlo models

Monte Carlo (MC) simulations are used to calculate acceptances and efficiencies for triggering, track reconstruction, event selection, lepton identification and background simulation. The elastic and proton-dissociative J/ψ signal events are generated using the program DIFFVM [28], which is based on Regge theory and the Vector Dominance Model [29]. For J/ψ production with proton dissociation a mass dependence of $\mathrm{d}\sigma/\mathrm{d}M_Y^2 \propto f(M_Y^2)M_Y^{-\beta}$ is implemented in DIFFVM. Here $f(M_Y^2) = 1$ for $M_Y^2 > 3.6\,\mathrm{GeV}^2$, whereas for lower values of M_Y^2 the production of excited nucleon states is taken into account explicitly. The description of the forward energy flow and the simulated $W_{\gamma p}$ and t dependences are improved by weighting the MC samples in $W_{\gamma p}$, t and M_Y according to a functional behaviour motivated by the triple pomeron model [30] for the proton-dissociative case. The reweighting model contains seven parameters, which are adjusted to the data [31]. QED radiation effects, which are particularly relevant for $J/\psi \to e^+e^-$ decays, are simulated with the program PHOTOS [32]. The non-resonant di-lepton background is estimated using the GRAPE generator [33], which simulates electroweak processes $ep \to eX\,\ell^+\ell^-$. Possible interference effects between di-lepton production via electroweak processes and J/ψ decays are ignored.

For all MC samples detector effects are simulated in detail with the GEANT program [34]. The MC description of the detector response, including trigger efficiencies, is adjusted using comparisons with independent data. Beam-induced backgrounds are taken into account by overlaying the simulated event samples with randomly triggered events. The simulated MC events are passed through the same reconstruction and analysis software as is used for the data.

2.3 Detector

The H1 detector is described in detail elsewhere [35, 36]. Only those components essential for this analysis are described here. The origin of the right-handed H1 coordinate system is the nominal ep interaction point, with the direction of the proton beam defining the positive z axis (forward direction). Transverse momenta are measured in the x-y plane. Polar (ϑ) and azimuthal (ϕ) angles are measured with respect to this frame of reference.

In the central region ($15^\circ < \vartheta < 165^\circ$) the interaction point is surrounded by the central tracking detector (CTD). The CTD comprises two large cylindrical jet chambers (CJC1 and CJC2) and a silicon vertex detector [37]. The CJCs are separated by a further drift chamber which improves the z coordinate reconstruction. The CTD detectors are arranged concentrically around the interaction region in a uniform solenoidal magnetic field of $1.16\,\mathrm{T}$. The trajectories of charged particles are measured with a transverse momentum resolution of $\sigma(p_T)/p_T \approx 0.2\%\, p_T/\mathrm{GeV} \oplus 1.5\%$. The CJCs also provide a measurement of the specific ionisation energy loss $\mathrm{d}E/\mathrm{d}x$ of charged particles with a relative resolution of 6.5% for long tracks.

The liquid argon (LAr) sampling calorimeter [38] surrounds the tracking chambers and has a polar angle coverage of $4^\circ < \vartheta < 154^\circ$. It consists of an inner electromagnetic section with lead absorbers and an outer hadronic section with steel absorbers. Energies of electromagnetic showers are measured with a precision of $\sigma(E)/E = 12\%/\sqrt{E/\,\mathrm{GeV}} \oplus 1\%$ and those of hadronic showers with $\sigma(E)/E = 50\%/\sqrt{E/\,\mathrm{GeV}} \oplus 2\%$, as determined in test beam experiments [39, 40]. In the backward region ($153^\circ < \vartheta < 178^\circ$), particle energies are measured by a lead-scintillating fibre spaghetti calorimeter (SpaCal) [36].

The calorimeters are surrounded by the muon system. The central muon detector (CMD) is integrated in the iron return yoke for the magnetic field and consists of 64 modules, which are grouped into the forward endcap, the forward and backward barrel and the backward endcap and cover the range $4^\circ \leq \vartheta \leq 171^\circ$.

Two sub-detectors situated in the forward direction are used in this analysis. These are the PLUG calorimeter, which is situated at $z = 4.9\,\mathrm{m}$, and consists of four double layers of scintillator and lead absorber, and the $z = 28\,\mathrm{m}$ station of the forward tagging system (FTS), which comprises scintillator counters situated around the beam-pipe.

H1 has a four-level trigger system. The first level trigger (L1) is based on fast signals from selected sub-detector components, which are combined and refined at the second level (L2). The third level (L3) is a software based trigger using combined L1 and L2 trigger information. After reading out the full event information events are reconstructed and subjected to an additional selection at a software filter farm (L4). The data used for this measurement were recorded using the Fast Track Trigger (FTT) [41] which, based on hit information provided by the CJCs, reconstructs tracks with subsequently refined granularity at the first two trigger levels, first in the x-y plane at L1 and then in three dimensions at L2.

For the data set taken at $\sqrt{s} \approx 318\,\mathrm{GeV}$ the luminosity is determined from the rate of the elastic QED Compton process $ep \to e\,\gamma p$, with the positron and the photon detected in the SpaCal calorimeter, and the rate of Deep-Inelastic Scattering (DIS) events measured in the SpaCal calorimeter [42]. For the data set taken at $\sqrt{s} \approx 225\,\mathrm{GeV}$ the luminosity determination is based on the measurement of the Bethe-Heitler process $ep \to e\,\gamma p$ where the photon is detected in a calorimeter located at $z = -104\,\mathrm{m}$ downstream of the interaction region in the electron beam direction.

2.4 Event selection

The measurement is based on two data sets, both recorded with a positron beam energy of $E_e = 27.6\,\mathrm{GeV}$. The first data set was taken in the years 2006 and 2007, when HERA was operated with a proton beam energy of 920 GeV, resulting in a centre-of-mass energy of $\sqrt{s} \approx 318$ GeV. It corresponds to an integrated luminosity of $\mathcal{L} = 130\,\mathrm{pb}^{-1}$. The second data set was recorded in the last months before the shutdown of HERA in 2007, when the proton beam had a reduced energy of 460 GeV, resulting in $\sqrt{s} \approx 225$ GeV. This data set corresponds to an integrated luminosity of $\mathcal{L} = 10.8\,\mathrm{pb}^{-1}$. These two samples will be referred to as high-energy (HE) and low-energy (LE) data sets in the following.

Photoproduction events are selected by requiring the absence of a high energy electromagnetic cluster, consistent with a signal from a scattered beam positron in the calorimeters. Events with positrons detected in the SpaCal or LAr calorimeter with with energy above $8\,\mathrm{GeV}$ are rejected. This limits the photon virtuality to $Q^2 \lesssim 2.5$ GeV^2, resulting in a mean virtuality of $\langle Q^2 \rangle = 0.1$ GeV^2.

The triggering of events relies on the online reconstruction of exactly two oppositely charged tracks with transverse momenta $p_T > 0.8\,$GeV by the FTT. This condition is verified offline using reconstructed tracks based on the full CTD information in the polar range $20^\circ < \vartheta < 165^\circ$.

Electrons from J/ψ decays are identified using an electron estimator D [43], which is based on energy deposits and shower shape variables in the LAr calorimeter and the specific ionisation energy loss $\mathrm{d}E/\mathrm{d}x$ measured in the CJCs. The estimator is defined such that $D = 1$ for genuine electrons and $D = 0$ for background from pions. The selection of $J/\psi \to e^+e^-$ events is performed by requiring a well identified electron with $D > 0.8$ in the polar range $20^\circ < \vartheta_e < 140^\circ$, and by observing a specific ionisation loss of the second track compatible with the electron hypothesis [31].

In the selection of $J/\psi \to \mu^+\mu^-$ events one muon candidate is identified either in the calorimeter or in the muon system in the polar angle range of $20^\circ < \vartheta_\mu < 162.5^\circ$ [31]. In order to reject misidentified $J/\psi \to e^+e^-$ events in this sample, the measured $\mathrm{d}E/\mathrm{d}x$ values of both tracks must be incompatible with the electron hypothesis [31]. The signature of a $J/\psi \to \mu^+\mu^-$ event can also be mimicked by a muon from a cosmic shower passing through the detector. The corresponding background is rejected by an acollinearity cut and a cut on the timing information from the CTD [31].

In order to suppress remaining non-ep background, the event vertex, which is reconstructed from the charged tracks in the event, is required to be within $35\,\mathrm{cm}$ of the nominal interaction point.

The summed squared energies of the SpaCal and LAr calorimeter clusters not related to the J/ψ decay and above $400\,$MeV have to satisfy the condition $\sum_i E_i^2 < 2.5\,\mathrm{GeV}^2$. This requirement reduces the remaining background from proton-dissociative J/ψ production with $M_Y > 10\,$GeV to less than 2% and from inelastic J/ψ production to the per-mille level [31].

The di-lepton invariant mass distributions as reconstructed from the tracks for the muon and the electron selection are shown in figure 2 for both the HE and LE samples. In all distributions the J/ψ peak at $m_{\ell\ell} \approx 3.1\,$GeV is clearly visible. The prominent tail of the mass peak in the $J/\psi \to e^+e^-$ channel towards low values of m_{ee} is due to QED radiation losses and bremsstrahlung from the electrons, reducing their momenta. There is also background from non-resonant QED processes $ep \to eX\, \ell^+\ell^-$. Non-resonant diffraction contributes as a background to the muon channel due to pions misidentified as muons. In contrast, the electron channel has negligible pion contamination near the J/ψ mass peak due to the superior background rejection of the electron selection.

2.5 Signal determination

2.5.1 $J/\psi \to \mu^+\mu^-$

For the muon decay channel the number of reconstructed J/ψ mesons is obtained from the invariant di-muon mass distributions $m_{\mu\mu}$ in bins of t_{rec} and $W_{\gamma p,rec}$. This is done by fitting the sum of a Student's t-function describing the signal and an exponential distribution for the non-resonant background with an extended binned log-likelihood fit using the RooFit package [44].

The fit model has the form

$$f(N_{\text{sig}}, N_{\text{BG}}, m_{\mu\mu}; \mu, \sigma, n, c) = N_{\text{sig}}\, p_{\text{sig}}(m_{\mu\mu}; \mu, \sigma, n) + N_{\text{BG}}\, p_{\text{BG}}(m_{\mu\mu}; c) \tag{1}$$

with free shape parameters μ, σ, n and c describing the probability density functions of the J/ψ signal p_{sig} and of the background p_{BG}. The number of signal and background events are given by N_{sig} and N_{BG}, respectively. The probability density functions are defined as

$$p_{\text{sig}}(m_{\mu\mu}) = n_{\text{sig}} \left(1 + \frac{r^2}{n}\right)^{-0.5(n+1)}, \quad r = (m_{\mu\mu} - \mu)/\sigma, \quad n > 0 \quad \text{and} \tag{2}$$

$$p_{\text{BG}}(m_{\mu\mu}) = n_{\text{BG}}\, e^{-c \cdot m_{\mu\mu}}. \tag{3}$$

The factors n_{sig} and n_{BG} are chosen such that the probability densities are normalised to one for both $p = p_{\text{sig}}$ and $p = p_{\text{BG}}$, in the fit range $2.3\,\text{GeV} < m_{\mu\mu} < 5\,\text{GeV}$. The small $\psi(2S)$ contribution is also included in the fit, modelled by a Gaussian.

The results of the fits to the di-muon samples are shown together with the data in figure 2. The fit yields to 29931 ± 217 $J/\psi \to \mu^+\mu^-$ events for the HE data set and 2266 ± 56 $J/\psi \to \mu^+\mu^-$ events for the LE data sets.

2.5.2 $J/\psi \to e^+e^-$

For the electron decay channel the signal is determined from the invariant di-electron mass distributions obtained in bins of t_{rec} and $W_{\gamma p,rec}$. To reconstruct the number of J/ψ mesons, a different procedure from that used in the muon channel is employed, which minimises the sensitivity to details of the large radiative tail of the J/ψ mass peak visible in figure 2 and discussed above. The non-resonant background, modelled using the QED process $ep \to eX\ \ell^+\ell^-$ as simulated with GRAPE, is subtracted from the data. This is possible due to the negligible contamination from particles other than electrons at and above the J/ψ mass peak. The normalisation of the simulated QED background is determined prior to the background subtraction by fitting the background to the overall invariant mass distribution in the mass window $3.75 < m_{ee} < 5\,\text{GeV}$ above the $\psi(2S)$ mass, where only the QED contribution is present. Within errors this normalisation factor is consistent with unity.

After background subtraction the remaining events are counted within a window of $2.3 < m_{ee} < 3.3\,\text{GeV}$ around the nominal J/ψ mass peak. This yields 23662 ± 177 $J/\psi \to e^+e^-$ events for the HE data set and 1760 ± 47 $J/\psi \to e^+e^-$ events for the LE data sets. These numbers of events are then corrected to account for the fraction of signal events outside the counting window, which is close to 5% as determined using the J/ψ MC simulation. Within the counting window the J/ψ MC simulation describes the behaviour of the radiative tail in the data well.

2.6 Experimental signatures of elastic and proton-dissociative processes

Proton-dissociative candidate events are identified by requiring either a large value of $|t_{rec}| \gtrsim 1.5\,\mathrm{GeV}^2$ or energy deposits in the H1 forward detectors, caused by fragments of the proton-dissociative system. Three subdetectors, situated at different locations, are used in this analysis to measure activity in the forward direction, using the following requirements.

- At least one cluster well above the noise level is found in the forward part of the LAr, with an energy above $400\,\mathrm{MeV}$ and $\vartheta < 10°$.
- The summed energy of all clusters in the PLUG calorimeter is above $4\,\mathrm{GeV}$, where all clusters above the threshold level of $1.2\,\mathrm{GeV}$ are considered.
- Activity is observed in at least one scintillator of the FTS station situated at $z = 28\,\mathrm{m}$.

If at least one of these conditions is fulfilled, the event is flagged as tagged. Identical tagging methods are applied in the e^+e^- and $\mu^+\mu^-$ channels.

In figure 3 the simulated tagging efficiencies and tagging fractions observed in data and simulation are shown as functions of $W_{\gamma p,rec}$ and $-t_{rec}$. The tagging fractions are obtained from the e^+e^- sample, and contain QED contributions in addition to di-electron events from diffractive J/ψ production. In order to enrich it with genuine J/ψ decays, the sample is restricted to invariant masses in the window $m_{ee} = 2.3 - 3.3\,\mathrm{GeV}$. The tagging fractions observed in the data are compared to the simulation. The simulation is based on the MC generators DIFFVM for elastic and proton-dissociative J/ψ production and GRAPE, which is used to describe the QED background. The uncertainty in the simulation due to the tagging of the forward energy flow is represented by the shaded bands. The tagging efficiency and fraction show a flat behaviour as a function of $W_{\gamma p,rec}$. A steep rise of the tagging fraction is observed as a function of t_{rec}, which reflects the relative elastic and proton-dissociative contribution in data.

An unambiguous event-by-event distinction between elastic and proton-dissociative events is not possible with the H1 detector. Proton-dissociative events can be misidentified as elastic events if the outgoing dissociated proton remains undetected due to the limited acceptance of the forward detectors. On the other hand, elastic events may have significant energy deposits in the forward detectors due to possible beam induced background and may be misidentified as proton-dissociative events. However, since the forward energy flow is modelled by the MC simulation, elastic and proton-dissociative cross sections can be unfolded on a statistical basis.

2.7 Unfolding

Regularised unfolding is used to determine the elastic and proton-dissociative cross sections in bins of t and $W_{\gamma p}$ from the number of events observed as a function of t_{rec} and $W_{\gamma p,rec}$, respectively, and from the tagging information as described in the previous subsection. The general procedure is described in [43, 45, 46] and the references therein. In the following only the aspects most relevant to this analysis are summarised; further details are discussed in [31].

All efficiency corrections and migration effects are described by a response matrix $\mathbf{A}$, which correlates the number of reconstructed J/ψ events in each analysis bin, represented by the vector $\boldsymbol{y}_{\mathrm{rec}}$, with the true distribution $\boldsymbol{x}_{\mathrm{true}}$ via the matrix equation $\boldsymbol{y}_{\mathrm{rec}} = \mathbf{A}\boldsymbol{x}_{\mathrm{true}}$. The matrix element A_{ij} gives the probability for an event originating from bin j of $\boldsymbol{x}_{\mathrm{true}}$ to be measured in bin i of $\boldsymbol{y}_{\mathrm{rec}}$. The unfolded "true" distribution is obtained from the measured one by minimising a χ^2-function $\chi^2(\boldsymbol{x}_{\mathrm{true}}; \boldsymbol{y}_{\mathrm{rec}})$ by variation of $\boldsymbol{x}_{\mathrm{true}}$, with a smoothness constraint determined by a regularisation parameter. This parameter is chosen such that the correlations in the covariance matrix of the unfolded distribution $\boldsymbol{x}_{\mathrm{true}}$ are minimised.

Two types of response matrix $\mathbf{A}$ are used: one to unfold differential cross sections as a function of t, and one to unfold differential cross sections as a function of $W_{\gamma p}$. The response matrices are calculated from the simulation and are defined such that the elastic and proton-dissociative differential cross sections are determined simultaneously. By using the tagging information for small values of $|t_{rec}| \lesssim 1.5\,\mathrm{GeV}^2$, the elastic and proton-dissociative cross sections are disentangled. Since the region of large values of $|t_{rec}|$ is completely dominated by proton dissociation, no tagging condition is applied. Further, two reconstructed bins are associated with each bin at the truth level, in order to provide sufficiently detailed information on the probability distribution and to improve the accuracy of the unfolding procedure.

The unfolding procedure is applied separately for the HE and the LE data sets. The response matrices for the LE data set are similar to those for the HE case. However they contain fewer bins due to the smaller number of events.

In figure 4 control distributions are shown for $W_{\gamma p,rec}$ and $-t_{rec}$ separately for the $\mu^+\mu^-$ sample and the e^+e^- sample. Both samples are restricted in $m_{\ell\ell}$ to the J/ψ peak region, which is chosen for the $\mu^+\mu^-$ sample to be $2.8 < m_{\mu\mu} < 3.3\,\mathrm{GeV}$. For the e^+e^- sample this region is enlarged to $2.3 < m_{ee} < 3.3\,\mathrm{GeV}$ in order not to cut into the radiative tail. The relative fractions of the elastic and proton-dissociative events simulated with DIFFVM as determined in the unfolding procedure, are also shown in figure 4. The contribution from the $\psi(2S)$ resonance is taken from the simulation, normalised using a previous measurement [20]. For the e^+e^- sample, the QED background simulated with GRAPE is indicated and normalised as described above. For the control distributions of the $\mu^+\mu^-$ sample the non-resonant background is subtracted from the data using a side band method [31]. This background contains a contribution from non-resonant diffractive events, due to pions misidentified as muons, in addition to the QED background. The data in all distributions are well described by the simulation.

2.8 Cross section determination and systematic uncertainties

The cross sections are measured for the kinematic ranges as defined in table 1. From the unfolded number of events in each signal bin i for the reaction $\gamma p \to J/\psi \to \ell\ell$, the bin-averaged cross sections are obtained as

$$\frac{\mathrm{d}\sigma(\gamma p \to J/\psi)}{\mathrm{d}t} = \frac{1}{\Phi_\gamma^T} \frac{N_{i,t,\ell\ell}}{\mathcal{L} \cdot \mathcal{B}(\ell\ell) \cdot \Delta t_i} \quad , \tag{4}$$

and

$$\sigma_{W_{\gamma p}}(\gamma p \to J/\psi) = \frac{1}{\Phi_\gamma^{T,i,W_{\gamma p}}} \frac{N_{i,W_{\gamma p},\ell\ell}}{\mathcal{L} \cdot \mathcal{B}(\ell\ell)} \quad , \tag{5}$$

Data Set	E_p	Process	Q^2	M_Y	$\|t\|$	$W_{\gamma p}$
HE	$920\,\mathrm{GeV}$	elas pdis	$< 2.5\,\mathrm{GeV}^2$	m_p $m_p - 10\,\mathrm{GeV}$	$< 1.2\,\mathrm{GeV}^2$ $< 8\,\mathrm{GeV}^2$	$40 - 110\,\mathrm{GeV}$
LE	$460\,\mathrm{GeV}$	elas pdis	$< 2.5\,\mathrm{GeV}^2$	m_p $m_p - 10\,\mathrm{GeV}$	$< 1.2\,\mathrm{GeV}^2$ $< 5^{(\star)},\, 8\,\mathrm{GeV}^2$	$25 - 80\,\mathrm{GeV}$

Table 1: Kinematic range of the analysis. The phase space for elastic and proton-dissociative J/ψ processes is indicated by elas and pdis, respectively. The high- and low-energy data sets are denoted by HE and LE. $^{(\star)}$ The phase space restriction is applied only for the $\mathrm{d}\sigma/\mathrm{d}t$ cross section measurement.

where the variable Φ_γ^T is the transverse polarised photon flux [28], $\Phi_\gamma^{T,i,W_{\gamma p}}$ the transverse polarised photon flux per $W_{\gamma p}$ bin, Δt_i the bin width in t, $\ell\ell = ee$ or $\mu\mu$ depending on the decay channel, $N_{i,t,\ell\ell}$ and $N_{i,W_{\gamma p},\ell\ell}$ are the numbers of unfolded signal events in the corresponding bins of t or $W_{\gamma p}$, $\mathcal{L}$ is the integrated luminosity, and $\mathcal{B}(ee) = 5.94\%$, $\mathcal{B}(\mu\mu) = 5.93\%$ are the J/ψ branching fractions [47].

The systematic uncertainties on the J/ψ cross section measurement are determined by implementing shifts due to each source of uncertainty in the simulation and propagating the resulting variations in the unfolding matrices to the result. Those uncertainties which are uncorrelated between the two decay modes are classified as individual systematic uncertainties, while the uncertainties correlated between the e^+e^- and $\mu^+\mu^-$ samples are referred to as common systematic uncertainties.

The individual systematic uncertainties are as follows.

Lepton identification The efficiency of the simulated muon identification is reweighed to agree with that determined from data. The efficiency was determined with a $J/\psi \to \mu^+\mu^-$ sample, selected with at least one identified muon. The second muon is then probed to evaluate the single muon identification efficiency. The uncertainty on these weights is determined from the remaining difference between the simulation compared to data [31]. The resulting uncertainty on the cross sections is 2% at most.

The cut value on the electron discriminator D is varied by ± 0.04 around its nominal value of 0.8, which covers the differences in the D-distribution between simulation and data. The uncertainty propagated to the cross section is below 2%.

Signal extraction The uncertainty on the number of signal events due to the fitting procedure of the $m_{\mu\mu}$ invariant mass distributions is determined by a bias study as described in [31] and is typically $\approx 1\%$ but can rise to $\approx 5\%$ for the lowest $W_{\gamma p}$ bin of the proton-dissociative cross section.

The uncertainty on the background subtraction procedure for the e^+e^- sample is estimated by determining the background normalisation factor with data at very low invariant di-electron masses m_{ee} and agreement with the default method is found within 20%. The corresponding variation on the background is propagated to the differential cross sections which vary between 3% for bins with a low background to 11% for bins with a higher background contribution.

Branching ratio The relative uncertainty on the branching ratio for the muon and electron decay channels is 1% [47].

The following systematic uncertainties are have components contributing to the channel-specific individual and the common systematic uncertainties.

Trigger The trigger efficiency is typically 80% and is taken from the simulation. The trigger simulation is verified by a comparison to data in a sample of J/ψ mesons in deep-inelastic-scattering triggered independently on the basis of the scattered beam positron. A small difference of 3% is observed between the data and the simulation for J/ψ events decaying into muons. This difference is accounted for by a corresponding upwards shift of the efficiency in the simulation. No such correction is necessary for electrons. The remaining uncertainty is estimated to be 2% uncorrelated between the e^+e^- and $\mu^+\mu^-$ samples, i.e. treated as individual uncertainties, and 2% correlated between the two decay channels, i.e. treated as a common uncertainty.

Track finding efficiency The uncertainty due to the track reconstruction efficiency in the CTD is estimated to be 1% per track [48]. For electron tracks an additional 1% is applied, to account for the different hit finding efficiency due to bremsstrahlung effects. Since the uncertainty on the track finding efficiency affects both selected tracks coherently, a common uncertainty of 2% is applied to both samples and an additional 2% is applied for the electron sample.

The following common systematic uncertainties are considered.

Tagging The systematic uncertainty arising from the tagging condition is estimated by varying separately the simulated tagging efficiency for each detector used. The variations cover any possible shift in the individual relative efficiency distributions, and are 20% for the condition from the forward LAr calorimeter, 5% for the PLUG and 1% for the FTS [31]. The resulting uncertainties on the cross sections are typically a few percent, but reach 30% at the highest $|t|$ values of the elastic $\mathrm{d}\sigma/\mathrm{d}t$ cross section.

Empty calorimeter The uncertainty on the cut ensuring an empty calorimeter is obtained by varying the maximum allowed $\sum_i E_i^2$ from $2.25\,\mathrm{GeV}^2$ to $2.75\,\mathrm{GeV}^2$ in the simulation. This results in an uncertainty of typically 5% for the proton-dissociative cross sections. For the elastic cross sections this variation is negligible for most bins, except for the highest bin in $|t|$, where it reaches to 13%.

MC modelling The model uncertainty in the MC simulation due to uncertainties in the dependences on t, $W_{\gamma p}$ and M_Y is determined by varying the fit parameters of the weighting procedure within the errors obtained in a dedicated fit of the forward energy flow [31]. For the cross section as a function of $W_{\gamma p}$ the corresponding uncertainties are below 4%, whereas for the cross sections differential in t, values around 10% are obtained for the high $|t|$ bins.

Luminosity The integrated luminosity is known to within $\pm 2.7\%$ for the HE data set and to within $\pm 4\%$ for the LE data set [42].

$\psi(2S)$ background Background from $\psi(2S)$ decays to $J/\psi\, X$ is estimated to contribute 4% to the selected J/ψ events, and is subtracted from the data prior to the unfolding procedure [20]. The cross section measurements are affected by an uncertainty of 1.5%.

Q^2 dependence The Q^2 dependence of the cross section is parametrised as $\sigma_{\gamma p} \propto \left(m_\psi^2 + Q^2\right)^{-n}$ [4]. The corresponding systematic uncertainty is obtained by varying the parameter n in the range 2.50 ± 0.09. The cross sections are affected by less than 1%.

The differential cross sections obtained from the electron and the muon data agree within uncertainties. The two measurements are combined by taking into account their individual uncertainties. This combination procedure involves the numerical minimisation of a standard χ^2 function including the full statistical error matrix and the correlated systematic errors with nuisance parameters, similar to that defined in [49, 50]. All individual uncertainties are incorporated within this procedure, whereas the common uncertainties are considered after the combination only. The consistency of the data sets can be verified by looking at the resulting nuisance parameters. None of the nuisance parameters shifts by more than one standard deviation.

Figure 5 shows the result of the combination for the elastic and proton-dissociative cross sections as a function of $W_{\gamma p}$. The input data obtained in the electron and muon decay channels are shown together with the combined data.

3 Results

The elastic and proton-dissociative differential J/ψ cross sections as functions of t and $W_{\gamma p}$ are measured in the kinematic ranges defined in table 1 using the decay channels $J/\psi \to \mu^+\mu^-$ and $J/\psi \to e^+e^-$.

Tables 4, 5 and 6 list the combined data points for all cross sections together with their uncertainties and all common systematic uncertainties. The input data to the combination procedure, including all individual systematic uncertainties together with the full covariance matrices of the combined results can be found in [51].

3.1 t dependence

Figure 6 shows the measured elastic and proton-dissociative cross sections differential in $-t$, separately for the LE and HE data sets. The cross sections fall steeply with increasing $-t$, and shows a clear difference between the shapes of the proton-dissociative and elastic distributions. The proton-dissociative cross section levels off for very low values of $|t|$. There is a phase space effect such that for small $|t|$ it is not possible to produce large masses of M_Y.

In figure 7 the proton-dissociative measurement from the HE data set as a function of $-t$ is compared to a previous analysis [24] covering the region of high $|t|$, which is completely dominated by proton-dissociative events. The high $|t|$ data [24] are adjusted to the $W_{\gamma p}$, Q^2 and M_Y ranges of the present analysis by applying a phase space correction of about 7%. Comparing the two measurements, the present proton-dissociative cross sections extend the reach to small values of $|t|$. In the overlap region $2 < |t| < 8\,\text{GeV}^2$ the two measurements agree.

The elastic and proton-dissociative differential cross sections $\mathrm{d}\sigma/\mathrm{d}t$ are fitted simultaneously, using a χ^2-function [49, 50] based on the error matrix obtained in the combination procedure and all common systematic uncertainties. The elastic cross section is parametrised as $\mathrm{d}\sigma/\mathrm{d}t = N_{el}\, e^{-b_{el}|t|}$. For the proton-dissociative cross section $\mathrm{d}\sigma/\mathrm{d}t = N_{pd}\,(1 + (b_{pd}/n)|t|)^{-n}$ is chosen, which interpolates between an exponential at low $|t|$ and a power law behaviour at high values of $|t|$. The fits are performed separately for the HE and the LE measurements. In the case of the HE data the previously measured high $|t|$ data are included in the fit. This fit yields a value of $\chi^2/\mathrm{NDF} = 26.6/18$ after excluding the two lowest t data points in both the elastic and the proton-dissociative channel. For fit of the LE data set, the parameter n is fixed to the value obtained from the HE data set, since the LE data are not precise enough to constrain b_{pd} and n simultaneously. The obtained parametrisations for the elastic and proton-dissociative cross sections are compared to the data in figure 6 and figure 7. Table 2 summarises the fit parameters and their uncertainties.

The elastic cross section data for $-t > 0.1\,\text{GeV}$ are well described by the exponential parametrisation. They fall much faster with increasing $|t|$ than the proton-dissociative cross section even at small $|t|$, which is reflected in the values for b_{el} and b_{pd}. The value extracted for b_{el} is compatible with previous results [4], although the previous fit was done as a function of $p^2_{T,J/\psi}$ rather than $-t$. Some difference between the b_{el} values for the LE and HE data is expected [4] due to the different ranges in $W_{\gamma p}$ corresponding to $\langle W_{\gamma p}\rangle = 78\,\text{GeV}$ for the HE data set and $\langle W_{\gamma p}\rangle = 55\,\text{GeV}$ for the LE data.

3.2 Energy dependence

The measured elastic and proton-dissociative cross sections as a function of $W_{\gamma p}$ are shown in figures 8. The elastic and proton-dissociative cross sections are of similar size at the lowest $W_{\gamma p} = 30$ GeV accessed in this analysis. The elastic cross section rises faster with increasing $W_{\gamma p}$ than the proton-dissociative one. The ratio of the proton-dissociative to the elastic cross section as a function of $W_{\gamma p}$ is also shown in figure 8. The ratio decreases from 1 to 0.8 as $W_{\gamma p}$ increases from 30 GeV to 100 GeV. When calculating the ratio no attempt is made to extrapolate the elastic measurement to $-t = 8\,\text{GeV}^2$. The corresponding correction is estimated to be smaller than 1%.

In figure 9 the elastic cross section measurements of this analysis are compared to previous measurements at HERA [4, 5]. The LE data extend the range accessible in $W_{\gamma p}$ to lower values when compared to previous H1 measurements [4]. The HE data have a large overlap with previous H1 measurements in the region $40\,\text{GeV} < W_{\gamma p} < 110\,\text{GeV}$ and show a similar precision. Within normalisation uncertainties, the previous measurements and the new data are in agreement.

Data period	Process	Parameter	Fit value	Correlation
HE	$\gamma p \rightarrow J/\psi\, p$	b_{el}	$(4.88 \pm 0.15)\,\mathrm{GeV}^{-2}$	$\rho(b_{el}, N_{el})$ = 0.50 $\rho(b_{el}, b_{pd})$ = 0.49 $\rho(b_{el}, n)$ =-0.21 $\rho(b_{el}, N_{pd})$=0.68
		N_{el}	$(305 \pm 17)\,\mathrm{nb/GeV}^2$	$\rho(N_{el}, b_{pd})$ = 0.23 $\rho(N_{el}, n)$ =-0.07 $\rho(N_{el}, N_{pd})$=0.46
	$\gamma p \rightarrow J/\psi\, Y$	b_{pd}	$(1.79 \pm 0.12)\,\mathrm{GeV}^{-2}$	$\rho(b_{pd}, n)$ =-0.78 $\rho(b_{pd}, N_{pd})$=0.76
		n	3.58 ± 0.15	$\rho(n, N_{pd})$=-0.46
		N_{pd}	$(87 \pm 10)\,\mathrm{nb/GeV}^2$	
LE	$\gamma p \rightarrow J/\psi\, p$	b_{el}	$(4.3 \pm 0.2)\,\mathrm{GeV}^{-2}$	$\rho(b_{el}, N_{el})$ = 0.37 $\rho(b_{el}, b_{pd})$ = 0.10 $\rho(b_{el}, N_{pd})$=0.41
		N_{el}	$(213 \pm 18)\,\mathrm{nb/GeV}^2$	$\rho(N_{el}, b_{pd})$ = -0.24 $\rho(N_{el}, N_{pd})$=-0.10
	$\gamma p \rightarrow J/\psi\, Y$	b_{pd}	$(1.6 \pm 0.2)\,\mathrm{GeV}^{-2}$	$\rho(b_{pd}, N_{pd})$=0.53
		n	3.58 (fixed value)	
		N_{pd}	$(62 \pm 12)\,\mathrm{nb/GeV}^2$	

Table 2: Parameter values obtained from the fits to the differential cross sections $\mathrm{d}\sigma/\mathrm{d}t$, including their errors and correlations. The fit functions are described in the text. HE and LE denote the high- and low-energy data sets, respectively.

The measured elastic and proton-dissociative cross sections as a function of $W_{\gamma p}$, shown in figure 8, are fitted simultaneously, taking into account the correlations between the proton-dissociative and the elastic cross sections. The fit also includes data from a previous measurement [4] shown in figure 8, with a normalisation uncertainty of 5% and all other systematic uncertainties treated as uncorrelated. As parametrisation two power law functions of the form $\sigma = N\,(W_{\gamma p}/W_{\gamma p,0})^{\delta}$ with $W_{\gamma p,0} = 90\,\mathrm{GeV}$ are used with separate sets of parameters for the elastic and the proton-dissociative cases. The χ^2-function is defined in the same manner as for fits of the t-dependences.

The result of the fit is compared to the measurements in figures 8 and in figures 9. The parametrisation describes the data well ($\chi^2/\mathrm{NDF} = 32.6/36$). The fitted parameters are given in table 3 together with their uncertainties and correlations. In Regge phenomenology the parameter δ can be related to the pomeron trajectory $\alpha(t) = \alpha(0) + \alpha' \cdot t$ by $\delta(t) = 4(\alpha(t) - 1)$. Using the values $\alpha'_{el} = 0.164 \pm 0.028 \pm 0.030\,\mathrm{GeV}^{-2}$ [4] and $\alpha'_{pd} = -0.0135 \pm 0.0074 \pm 0.0051\,\mathrm{GeV}^{-2}$ [24], together with the mean values of t for the elastic and proton-dissociative measurements, $\langle t \rangle = -0.2\,\mathrm{GeV}^2$ and $\langle t \rangle = -1.1\,\mathrm{GeV}^2$, one can estimate $\alpha(0)$ for the elastic and proton-dissociative process from these measured parameters. The obtained values of $\alpha(0)_{el} = 1.20 \pm 0.01$ and $\alpha(0)_{pd} = 1.09 \pm 0.02$ are in agreement with the results from [4,5,52].

The direct comparison between δ_{el} and δ_{pd} is made by looking at the ratio of the two cross sections, shown in figure 8. The ratio is parametrised as $N_R\,(W_{\gamma p}/W_{\gamma p,0})^{\delta_R}$ with $W_{\gamma p,0} =$

$90\,\mathrm{GeV}$, $N_R = N_{pd}/N_{el} = 0.81 \pm 0.10$ and $\delta_R = \delta_{pd} - \delta_{el} = -0.25 \pm 0.06$, taking all correlations into account. Qualitatively the decrease of this ratio with increasing $W_{\gamma p}$ has been predicted in [8] as a consequence of the non-unit and $W_{\gamma p}$ dependant survival probability for the proton dissociation process.

In figure 10 a compilation of cross section measurements for the elastic J/ψ cross section is shown as a function of $W_{\gamma p}$. The LE data from the present analysis close the gap to data from fixed target experiments[1] [26, 27] at low $W_{\gamma p}$. The fixed target data exhibit a lower normalisation and a steeper slope than observed at HERA. Also shown are recent results from the LHCb experiment [53]. The extrapolated fit function for the elastic J/ψ cross section is able to describe the LCHb data points at high $W_{\gamma p}$ well.

Following [14] the obtained value of δ can for large photon-proton centre-of-mass energies, $W_{\gamma p} \gg m_{J/\psi}$, be related to a leading-order gluon-density parametrised as $x \cdot g(x, \mu^2) = N \cdot x^{-\lambda}$ via $\delta_{el} \approx 4 \cdot \lambda$. The scale of J/ψ photoproduction is often taken to be $\mu^2 = 2.4\,\mathrm{GeV}^2$. The observed value $\lambda_{J/\psi} = 0.168 \pm 0.008$ is in remarkable agreement with $\lambda_{incl}(Q^2 = 2.5\,\mathrm{GeV}^2) = 0.166 \pm 0.006$ obtained from fits to inclusive DIS cross sections [49]. Skewing effects [14, 54] are ignored in this comparison.

In [14] both a leading order and a next-to-leading order gluon-density are derived, via fits to previous J/ψ measurements at HERA [4, 21–23]. The fit results obtained in [14] are compared with the data in figure 11. Both fits are also extrapolated from the $W_{\gamma p}$ range of the input data to higher $W_{\gamma p}$ and compared with the LHCb measurement. The leading-order fit describes the LHCb data well, whereas the next-to-leading order fit lies above the LHCb cross sections.

Process	Parameter	Fit value	Correlation
$\gamma p \to J/\psi\, p$	δ_{el}	0.67 ± 0.03	$\rho(\delta_{el}, N_{el})$ =-0.08 $\rho(\delta_{el}, \delta_{pd})$ = 0.01 $\rho(\delta_{el}, N_{pd})$=0.09
	N_{el}	$81 \pm 3\,\mathrm{nb}$	$\rho(N_{el}, \delta_{pd})$ = -0.27 $\rho(N_{el}, N_{pd})$=-0.18
$\gamma p \to J/\psi\, Y$	δ_{pd}	0.42 ± 0.05	$\rho(\delta_{pd}, N_{pd})$=0.09
	N_{pd}	$66 \pm 7\,\mathrm{nb}$	
Ratio	$\delta_R = \delta_{pd} - \delta_{el}$	-0.25 ± 0.06	$\rho(\delta_r, N_R)$=0.14
	$N_R = N_{pd}/N_{el}$	0.81 ± 0.11	

Table 3: Parameter values obtained from the fit to the cross sections as a function of $W_{\gamma p}$, including their errors and correlations. The fit functions are described in the text. The parameters for the ratio of the two functions are also given.

[1]The data from [26] and [27] have been updated using recent measurements of branching ratios [47]. The data from [26] are also corrected for contributions from inelastic processes, see [51] for more details.

4 Summary

Photoproduction cross sections for elastic and proton-dissociative diffractive J/ψ meson production have been measured as a function of t, the four-momentum transfer at the proton vertex, and as a function of $W_{\gamma p}$, the photon proton centre-of-mass energy in the kinematic ranges $|t| < 8\,\mathrm{GeV}^2$, $25\,\mathrm{GeV} < W_{\gamma p} < 110\,\mathrm{GeV}$ and for the proton-dissociative case $M_Y < 10\,\mathrm{GeV}$. The data were collected in positron-proton collisions with the H1 detector at HERA, at a centre-of-mass energy of $\sqrt{s} \approx 318$ GeV and $\sqrt{s} \approx 225$ GeV. Measurements in the electron and muon decay channels are combined, and are parametrised using phenomenological fits.

The elastic and the proton-dissociative cross sections are extracted simultaneously. Using this technique, a precise measurement of proton-dissociative J/ψ production was performed in the range of small $|t|$ for the first time. The data taken at low centre-of-mass energies close the gap between previous H1 measurements and fixed target data.

The data agree well with previous HERA measurements and with a model based on two gluon exchange. The $W_{\gamma p}$-dependence of the proton-dissociative channel is found to be significantly weaker than that of the elastic channel.

5 Acknowledgements

We are grateful to the HERA machine group whose outstanding efforts have made this experiment possible. We thank the engineers and technicians for their work in constructing and maintaining the H1 detector, our funding agencies for financial support, the DESY technical staff for continual assistance and the DESY directorate for support and for the hospitality which they extend to the non-DESY members of the collaboration. We would like to give credit to all partners contributing to the WLCG computing infrastructure for their support for the H1 Collaboration.

References

[1] P. D. B. Collins, "An Introduction to Regge Theory and High Energy Physics," Cambridge University Press, 1977.

[2] A. Donnachie and P. V. Landshoff, Phys. Lett. B **348** (1995) 213 [hep-ph/9411368].

[3] A. Levy, "Low x physics at HERA," Lecture Notes in Physics, **496**, (1997), 347-477, DESY-97-013, TAUP-2398-96.

[4] A. Aktas *et al.* [H1 Collaboration], Eur. Phys. J. C **46** (2006) 585 [hep-ex/0510016].

[5] S. Chekanov *et al.* [ZEUS Collaboration], Eur. Phys. J. C **24** (2002) 345 [hep-ex/0201043].

[6] V. A. Khoze, A. D. Martin and M. G. Ryskin, Phys. Lett. B **643** (2006) 93 [hep-ph/0609312].

[7] E. G. S. Luna *et al.*, Eur. Phys. J. C **59** (2009) 1 [arXiv:0807.4115].

[8] E. Gotsman *et al.*, Eur. Phys. J. C **52** (2007) 295 [hep-ph/0702053].

[9] M. G. Ryskin, Z. Phys. C **57** (1993) 89.

[10] S. J. Brodsky *et al.*, Phys. Rev. D **50** (1994) 3134 [hep-ph/9402283].

[11] D. Y. Ivanov *et al.*, Eur. Phys. J. C **34** (2004) 297 [hep-ph/0401131].

[12] N. Brambilla *et al.*, Eur. Phys. J. C **71** (2011) 1534 [arXiv:1010.5827].

[13] T. Teubner, hep-ph/9910329.

[14] A. D. Martin *et al.*, Phys. Lett. B **662** (2008) 252 [arXiv:0709.4406].

[15] M. Diehl, Phys. Rept. **388** (2003) 41 [hep-ph/0307382].

[16] L. Frankfurt, M. McDermott and M. Strikman, JHEP **0103** (2001) 045 [hep-ph/0009086].

[17] A. Caldwell and H. Kowalski, Phys. Rev. C **81** (2010) 025203.

[18] S. Aid *et al.* [H1 Collaboration], Nucl. Phys. B **472** (1996) 3 [hep-ex/9603005].

[19] C. Adloff *et al.* [H1 Collaboration], Phys. Lett. B **483** (2000) 23 [hep-ex/0003020].

[20] C. Adloff *et al.* [H1 Collaboration], Phys. Lett. B **541** (2002) 251 [hep-ex/0205107].

[21] J. Breitweg *et al.* [ZEUS Collaboration], Z. Phys. C **75** (1997) 215 [hep-ex/9704013].

[22] J. Breitweg *et al.* [ZEUS Collaboration], Eur. Phys. J. C **6** (1999) 603 [hep-ex/9808020].

[23] S. Chekanov *et al.* [ZEUS Collaboration], Nucl. Phys. B **695** (2004) 3 [hep-ex/0404008].

[24] A. Aktas *et al.* [H1 Collaboration], Phys. Lett. B **568** (2003) 205 [hep-ex/0306013].

[25] S. Chekanov *et al.* [ZEUS Collaboration], JHEP **1005** (2010) 085 [arXiv:0910.1235].

[26] M. E. Binkley *et al.*, Phys. Rev. Lett. **48** (1982) 73.

[27] B. H. Denby *et al.*, Phys. Rev. Lett. **52** (1984) 795.

[28] B. List and A. Mastroberardino, “DIFFVM - A Monte Carlo generator for diffractive processes in ep scattering,”, Proc. of the Workshop on Monte Carlo Generators for HERA Physics, eds. A.T. Doyle et al., DESY-PROC-1999-02 (1999) 396.

[29] J. J. Sakurai, Annals Phys. **11** (1960) 1;
M. Gell-Mann and F. Zachariasen, Phys. Rev. **124** (1961) 953;
T. H. Bauer *et al.*, Rev. Mod. Phys. **50** (1978) 261 [Erratum-ibid. **51** (1979) 407].

[30] N. P. Zotov, and V. A. Tsarev, Sov. Phys. Usp. **31** (1988) 119

[31] F. Huber, “Elastic and proton-dissociative J/ψ Photoproduction at low $W_{\gamma p}$ with the H1 Detector at HERA”, Ph.D. thesis, Universität Heidelberg (2012), DESY-THESIS-2013-004 (available at http://www-h1.desy.de/psfiles/theses/).

[32] E. Barberio and Z. Was, Comput. Phys. Commun. **79** (1994) 291;
Z. Was, P. Golonka and G. Nanava, PoS ACAT (2007) 071 [arXiv:0707.3044].

[33] T. Abe, Comput. Phys. Commun. **136** (2001) 126 [hep-ph/0012029].

[34] GEANT 3, R. Brun *et al.*, “Geant3,” CERN-DD/EE/84-1 (1987).

[35] I. Abt *et al.*, [H1 Collaboration], Nucl. Instr. and Meth. A **386** (1997) 310; ibid, 348.

[36] R.D. Appuhn *et al.*, Nucl. Instrum. Meth. A **386** (1997) 397.

[37] D. Pitzl *et al.*, Nucl. Instrum. Meth. A **454** (2000) 334 [hep-ex/0002044].

[38] B. Andrieu *et al.* [H1 Calorimeter Group], Nucl. Instrum. Meth. A **336** (1993) 460.

[39] B. Andrieu *et al.* [H1 Calorimeter Group], Nucl. Instrum. Meth. A **350** (1994) 57.

[40] B. Andrieu *et al.* [H1 Calorimeter Group], Nucl. Instrum. Meth. A **336** (1993) 499.

[41] A. Baird *et al.*, IEEE Trans. Nucl. Sci. 48 (2001) 1276 [hep-ex/0104010];
D. Meer *et al.*, IEEE Trans.Nucl.Sci., **49**, (2002) 357;
N. Berger *et al.*, IEEE Nuclear Science Symposium Conference Record, volume 3, (2004) 1976.

[42] F. D. Aaron *et al.* [H1 Collaboration], Eur. Phys. J. C **72** (2012) 2163 [arXiv:1205.2448].

[43] F. D. Aaron *et al.* [H1 Collaboration], Eur. Phys. J. C **72** (2012) 2148 [arXiv:1206.4346].

[44] W. Verkerke and D. P. Kirkby, eConf C **0303241** (2003) MOLT007 [physics/0306116].

[45] F. D. Aaron *et al.* [H1 Collaboration], Eur. Phys. J. C **66** (2010) 17 [arXiv:0910.5631].

[46] F. D. Aaron *et al.* [H1 Collaboration], Eur. Phys. J. C **72** (2012) 1970 [arXiv:1111.0584].

[47] J. Beringer *et al.* [Particle Data Group Collaboration], Phys. Rev. D **86** (2012) 010001.

[48] M. Brinkmann, “Measurement of the $D^{*\pm}$ Meson Production Cross Section and $F_2^{c\bar{c}}$ at High Q^2 in *ep* Scattering at HERA”, Ph.D. thesis, University Hamburg (2010), DESY-THESIS-2010-016 (available at http://www-h1.desy.de/psfiles/theses/).

[49] F. D. Aaron *et al.* [H1 Collaboration], Eur. Phys. J. C **63** (2009) 625 [arXiv:0904.0929].

[50] F. D. Aaron *et al.* [H1 and ZEUS Collaborations], JHEP **1001** (2010) 109 [arXiv:0911.0884].

[51] Additional material of this analysis is provided at URL
http://www-h1.desy.de/publications/H1publication.short_list.html

[52] F. D. Aaron *et al.* [H1 Collaboration], JHEP **1005** (2010) 032 [arXiv:0910.5831].

[53] R. Aaij *et al.* [LHCb Collaboration], J. Phys. G **40** (2013) 045001 [arXiv:1301.7084].

[54] L. Favart, M. V. T. Machado and L. Schoeffel, hep-ph/0511069.

[55] G. D. Lafferty and T. R. Wyatt, Nucl. Instrum. Meth., **A355** (1995) 541.

$W_{\gamma p}$ range [GeV]	$\langle W_{\gamma p}^{\rm bc}\rangle$ [GeV]	Φ_γ^T	$\sigma\left(\langle W_{\gamma p}^{\rm bc}\rangle\right)$ [nb]	$\Delta_{\rm tot}$ [nb]	$\Delta_{\rm comb}$ [nb]	$\rho_{\rm comb}^{\rm GC}$ [%]	$\delta_{\rm sys}^{\rm Trk,corr}$ [%]	$\delta_{\rm sys}^{\rm Trg,corr}$ [%]	$\delta_{\rm sys}^{\rm 2S}$ [%]	$\delta_{\rm sys}^{\mathcal{L}_H}$ [%]	$\delta_{\rm sys}^{\mathcal{L}_L}$ [%]	$\delta_{\rm sys}^{\rm LAr10}$ [%]	$\delta_{\rm sys}^{\rm PLUG}$ [%]	$\delta_{\rm sys}^{\rm FTS}$ [%]	$\delta_{\rm sys}^{\rm MC\ Model}$ [%]	$\delta_{\rm sys}^{Q^2}$ [%]	$\delta_{\rm sys}^{\rm R_{LT}}$ [%]	$\delta_{\rm sys}^{\rm EC}$ [%]
High energy data period for elastic J/ψ production																		
40.0 - 46.5	43.2	0.0158	50.7	4.9	2.1	62	2.0	2.0	1.5	2.7	-	-2.6	0.6	-0.1	-7.1	-0.1	0.0	1.4
46.5 - 53.5	50.0	0.0144	59.5	5.8	2.2	69	2.0	2.0	1.5	2.7	-	-2.6	0.6	-0.1	-7.3	-0.1	0.0	1.4
53.5 - 61.2	57.3	0.0131	61.8	6.2	2.7	71	2.0	2.0	1.5	2.7	-	-2.6	0.6	-0.1	-7.4	-0.1	0.0	1.4
61.2 - 69.4	65.3	0.0120	67.6	6.2	2.5	71	2.0	2.0	1.5	2.7	-	-2.6	0.6	-0.1	-6.6	-0.1	0.0	1.4
69.4 - 78.4	73.9	0.0112	72.4	6.4	2.6	71	2.0	2.0	1.5	2.7	-	-2.6	0.6	-0.1	-6.3	-0.1	0.0	1.4
78.4 - 88.0	83.2	0.0103	79.9	7.0	3.0	69	2.0	2.0	1.5	2.7	-	-2.6	0.6	-0.1	-6.0	-0.1	0.0	1.4
88.0 - 98.5	93.3	0.0096	84.4	7.0	3.0	69	2.0	2.0	1.5	2.7	-	-2.6	0.6	-0.1	-5.5	-0.1	0.0	1.4
98.5 - 110.0	104.3	0.0089	86.7	7.3	3.7	65	2.0	2.0	1.5	2.7	-	-2.6	0.6	-0.1	-5.2	-0.1	0.0	1.4
High energy data period for proton dissociative J/ψ production																		
40.0 - 46.5	43.2	0.0158	46.0	6.0	2.3	54	2.0	2.0	1.5	2.7	-	9.4	-2.2	0.5	-3.9	0.1	0.0	-4.3
46.5 - 53.5	50.0	0.0144	52.1	6.5	2.3	61	2.0	2.0	1.5	2.7	-	9.4	-2.2	0.5	2.5	0.1	0.0	-4.3
53.5 - 61.2	57.3	0.0131	58.7	7.4	2.3	61	2.0	2.0	1.5	2.7	-	9.4	-2.2	0.5	3.5	0.1	0.0	-4.3
61.2 - 69.4	65.3	0.0120	58.7	7.5	2.2	63	2.0	2.0	1.5	2.7	-	9.4	-2.2	0.5	4.6	0.1	0.0	-4.3
69.4 - 78.4	73.9	0.0112	61.5	8.0	2.4	62	2.0	2.0	1.5	2.7	-	9.4	-2.2	0.5	4.8	0.1	0.0	-4.3
78.4 - 88.0	83.2	0.0103	67.7	8.7	2.6	60	2.0	2.0	1.5	2.7	-	9.4	-2.2	0.5	4.6	0.1	0.0	-4.3
88.0 - 98.5	93.3	0.0096	69.8	9.0	2.7	59	2.0	2.0	1.5	2.7	-	9.4	-2.2	0.5	4.8	0.1	0.0	-4.3
98.5 - 110.0	104.2	0.0089	68.8	9.0	3.0	54	2.0	2.0	1.5	2.7	-	9.4	-2.2	0.5	4.6	0.1	0.0	-4.3
Low energy data period for elastic J/ψ production																		
25.0 - 39.0	31.9	0.0465	39.7	4.9	3.4	62	2.0	2.0	1.5	-	4.0	-3.4	0.8	-0.1	-6.4	-0.1	0.0	1.9
39.0 - 57.0	47.9	0.0359	55.4	5.6	3.3	64	2.0	2.0	1.5	-	4.0	-3.4	0.8	-0.1	-5.1	-0.1	0.0	1.9
57.0 - 80.0	68.4	0.0284	66.4	6.8	4.3	64	2.0	2.0	1.5	-	4.0	-3.4	0.8	-0.1	-4.7	-0.1	0.0	1.9
Low energy data period for proton dissociative J/ψ production																		
25.0 - 39.0	31.9	0.0465	42.0	8.1	4.8	59	2.0	2.0	1.5	-	4.0	12.0	-2.9	0.3	-4.6	0.1	0.0	-6.4
39.0 - 57.0	47.9	0.0359	55.1	9.4	4.5	59	2.0	2.0	1.5	-	4.0	12.0	-2.9	0.3	-2.5	0.1	0.0	-6.4
57.0 - 80.0	68.3	0.0284	62.0	10.7	5.3	57	2.0	2.0	1.5	-	4.0	12.0	-2.9	0.3	2.5	0.1	0.0	-6.4

Table 4: Elastic and proton-dissociative photoproduction cross sections $\sigma\left(\langle W_{\gamma p}^{\rm bc}\rangle\right)$ derived from the high- and low-energy data sets as a function of the photon proton centre-of-mass energy $W_{\gamma p}$ for the processes $ep \rightarrow e\, J/\psi\, Y$, where Y denotes either a proton p or a proton-dissociative system of mass $m_p < M_Y < 10\,$GeV. These cross sections are obtained after the combination of the cross sections from the $\mu^+\mu^-$ and e^+e^- decay channels and for the phase space as defined in table 1. $\langle W_{\gamma p}^{\rm bc}\rangle$ indicates the bin centres [55] and Φ_γ^T is the transverse polarised photon flux per bin. $\Delta_{\rm tot}$ and $\Delta_{\rm comb}$ denote the total and the combined statistical and channel-specific individual uncertainties, as obtained from the data combination, respectively. The global correlation coefficients ρ_{GC} are also shown. The full covariance matrix can be found in [51]. The remaining columns list the bin-to-bin correlated systematic uncertainties corresponding to a $+1\sigma$ shift due to the correlated tracking uncertainty $\delta_{\rm sys}^{\rm Trk,corr}$, the correlated triggering uncertainty $\delta_{\rm sys}^{\rm Trg,corr}$, the uncertainty from $\psi(2S)$ contributions $\delta_{\rm sys}^{\rm 2S}$, the integrated luminosities of the high- and low-energy data sets $\delta_{\rm sys}^{\mathcal{L}_H}$, $\delta_{\rm sys}^{\mathcal{L}_L}$, the tagging uncertainties in the LAr $\delta_{\rm sys}^{\rm LAr10}$, the plug $\delta_{\rm sys}^{\rm PLUG}$ and the FTS $\delta_{\rm sys}^{\rm FTS}$, due to the modelling of the MC $\delta_{\rm sys}^{\rm MC\ Model}$, the Q^2 dependance $\delta_{\rm sys}^{Q^2}$ and the cut on the empty calorimeter $\delta_{\rm sys}^{\rm EC}$.

$\lvert t\rvert$ range [GeV^2]	$\langle \lvert t\rvert^{\mathrm{bc}} \rangle$ [GeV^2]	$\frac{d\sigma}{d\lvert t\rvert}\left(\langle \lvert t\rvert^{\mathrm{bc}}\rangle\right)$ [nb/GeV^2]	Δ_{tot} [nb/GeV^2]	Δ_{comb} [nb/GeV^2]	$\rho^{\mathrm{GC}}_{\mathrm{comb}}$ [%]	$\delta^{\mathrm{Trk,corr}}_{\mathrm{sys}}$ [%]	$\delta^{\mathrm{Trg,corr}}_{\mathrm{sys}}$ [%]	$\delta^{\mathrm{2S}}_{\mathrm{sys}}$ [%]	$\delta^{\mathcal{L}_H}_{\mathrm{sys}}$ [%]	$\delta^{\mathrm{LAr10}}_{\mathrm{sys}}$ [%]	$\delta^{\mathrm{PLUG}}_{\mathrm{sys}}$ [%]	$\delta^{\mathrm{FTS}}_{\mathrm{sys}}$ [%]	$\delta^{\mathrm{MC\ Model}}_{\mathrm{sys}}$ [%]	$\delta^{Q^2}_{\mathrm{sys}}$ [%]	$\delta^{\mathrm{R_{LT}}}_{\mathrm{sys}}$ [%]	$\delta^{\mathrm{EC}}_{\mathrm{sys}}$ [%]
High energy data period for elastic J/ψ production																
0.00 - 0.05	0.02	336	18	11	70	2.0	2.0	1.5	2.7	-1.0	0.2	-0.1	-0.6	-0.1	0.0	0.5
0.05 - 0.11	0.08	240.5	12.9	7.2	71	2.0	2.0	1.5	2.7	-1.2	0.3	-0.1	-0.7	-0.1	0.0	0.6
0.11 - 0.17	0.14	161.2	9.3	5.5	66	2.0	2.0	1.5	2.7	-1.6	0.3	-0.1	-1.0	-0.1	0.0	0.8
0.17 - 0.25	0.21	111.4	7.0	4.1	62	2.0	2.0	1.5	2.7	-2.2	0.5	-0.1	-1.4	-0.1	0.0	1.0
0.25 - 0.35	0.30	70.4	5.1	3.2	61	2.0	2.0	1.5	2.7	-2.9	0.6	-0.2	-1.9	-0.1	0.0	1.4
0.35 - 0.49	0.41	41.2	3.7	2.2	59	2.0	2.0	1.5	2.7	-4.6	1.0	-0.3	-3.0	0.0	0.0	2.3
0.49 - 0.69	0.58	18.0	2.7	1.4	59	2.0	2.0	1.5	2.7	-9.2	2.1	-0.6	-6.5	0.1	0.0	4.7
0.69 - 1.20	0.90	4.83	1.75	0.67	72	2.0	2.0	1.5	2.7	-24.0	5.8	-1.4	-18.0	0.8	0.0	13.0
High energy data period for proton dissociative J/ψ production																
0.00 - 0.20	0.10	47.3	6.7	2.3	63	2.0	2.0	1.5	2.7	11.0	-2.2	0.6	3.6	-0.1	0.0	-4.6
0.20 - 0.40	0.29	43.8	6.0	1.9	64	2.0	2.0	1.5	2.7	11.0	-2.4	0.6	2.2	-0.0	0.0	-4.7
0.40 - 0.64	0.52	36.7	5.1	1.6	70	2.0	2.0	1.5	2.7	11.0	-2.6	0.7	2.0	-0.1	0.0	-5.0
0.64 - 0.93	0.78	27.8	4.2	1.3	74	2.0	2.0	1.5	2.7	12.0	-2.9	0.7	2.8	-0.1	0.0	-5.7
0.93 - 1.31	1.12	16.80	2.59	0.87	63	2.0	2.0	1.5	2.7	12.0	-3.1	0.7	2.0	-0.1	0.0	-5.9
1.31 - 1.83	1.55	10.05	1.56	0.52	49	2.0	2.0	1.5	2.7	12.0	-3.1	0.5	1.7	0.0	0.0	-6.2
1.83 - 2.63	2.21	6.04	0.68	0.33	46	2.0	2.0	1.5	2.7	6.0	-1.7	0.3	-5.5	0.5	0.0	-3.0
2.63 - 4.13	3.30	2.80	0.38	0.16	42	2.0	2.0	1.5	2.7	6.7	-1.9	0.3	-8.7	0.5	0.0	-3.6
4.13 - 8.00	5.71	0.875	0.178	0.064	30	2.0	2.0	1.5	2.7	9.0	-2.5	0.3	-15.0	0.2	0.0	-5.4

Table 5: Elastic and proton-dissociative photoproduction cross sections derived from the high-energy data sets as a function of the squared four-momentum transfer at the proton vertex t, for the processes $ep \to eJ/\psi\, Y$, where Y denotes either a proton p or a proton-dissociative system of mass $m_p < M_Y < 10\,\mathrm{GeV}$. These cross sections are obtained after the combination of the cross sections from the $\mu^+\mu^-$ and e^+e^- decay channels and for the phase space as defined in table 1. $\langle \lvert t\rvert^{\mathrm{bc}} \rangle$ indicates the bin centres [55]. The transverse polarised photon flux Φ^T_γ for the given phase space range is 0.0953. See caption of table 4 for more dietails.

$\lvert t\rvert$ range [GeV^2]	$\langle \lvert t\rvert^{\mathrm{bc}} \rangle$ [GeV^2]	$\frac{d\sigma}{d\lvert t\rvert}\left(\langle \lvert t\rvert^{\mathrm{bc}}\rangle\right)$ [nb/GeV^2]	Δ_{tot} [nb/GeV^2]	Δ_{comb} [nb/GeV^2]	$\rho^{\mathrm{GC}}_{\mathrm{comb}}$ [%]	$\delta^{\mathrm{Trk,corr}}_{\mathrm{sys}}$ [%]	$\delta^{\mathrm{Trg,corr}}_{\mathrm{sys}}$ [%]	$\delta^{\mathrm{2S}}_{\mathrm{sys}}$ [%]	$\delta^{\mathcal{L}_L}_{\mathrm{sys}}$ [%]	$\delta^{\mathrm{LAr10}}_{\mathrm{sys}}$ [%]	$\delta^{\mathrm{PLUG}}_{\mathrm{sys}}$ [%]	$\delta^{\mathrm{FTS}}_{\mathrm{sys}}$ [%]	$\delta^{\mathrm{MC\ Model}}_{\mathrm{sys}}$ [%]	$\delta^{Q^2}_{\mathrm{sys}}$ [%]	$\delta^{\mathrm{R_{LT}}}_{\mathrm{sys}}$ [%]	$\delta^{\mathrm{EC}}_{\mathrm{sys}}$ [%]
Low energy data period for elastic J/ψ production																
0.00 - 0.11	0.05	178	16	12	49	2.0	2.0	1.5	4.0	-2.0	0.4	-0.1	-1.4	-0.1	0.0	1.0
0.11 - 0.25	0.17	99.6	9.4	7.0	52	2.0	2.0	1.5	4.0	-3.0	0.7	-0.1	-1.4	-0.1	0.0	1.5
0.25 - 0.47	0.35	43.7	5.6	4.3	53	2.0	2.0	1.5	4.0	-5.0	1.1	-0.1	-3.4	-0.0	0.0	2.6
0.47 - 1.20	0.75	9.7	1.8	1.3	57	2.0	2.0	1.5	4.0	-9.8	2.2	-0.3	-4.8	0.1	0.0	5.3
Low energy data period for proton dissociative J/ψ production																
0.00 - 0.50	0.23	42.8	7.5	3.5	63	2.0	2.0	1.5	4.0	13.0	-2.9	0.4	2.1	-0.1	0.0	-6.1
0.50 - 1.15	0.80	18.9	4.0	1.8	58	2.0	2.0	1.5	4.0	16.0	-3.7	0.5	-0.6	-0.0	0.0	-8.3
1.15 - 2.30	1.67	8.58	1.54	0.84	36	2.0	2.0	1.5	4.0	11.0	-2.8	0.2	-5.9	0.2	0.0	-6.2
2.30 - 5.00	3.42	2.01	0.58	0.36	21	2.0	2.0	1.5	4.0	8.9	-2.4	0.1	-19.0	0.8	0.0	-5.4

Table 6: Elastic and proton-dissociative photoproduction cross sections of the low-energy data sets as a function of the squared four-momentum transfer at the proton vertex t, for the processes $ep \to J/\psi\, Y$, where Y denotes either a proton p or a proton-dissociative system of mass $M_Y > m_p$. These cross sections are obtained after the combination of the cross sections from the $\mu^+\mu^-$ and e^+e^- decay channels and for the phase space as defined in table 1. $\langle \lvert t\rvert^{\mathrm{bc}} \rangle$ indicates the bin centres [55]. The transverse polarised photon flux Φ^T_γ for the given phase space range is 0.1108. See caption of table 4 for more dietails.

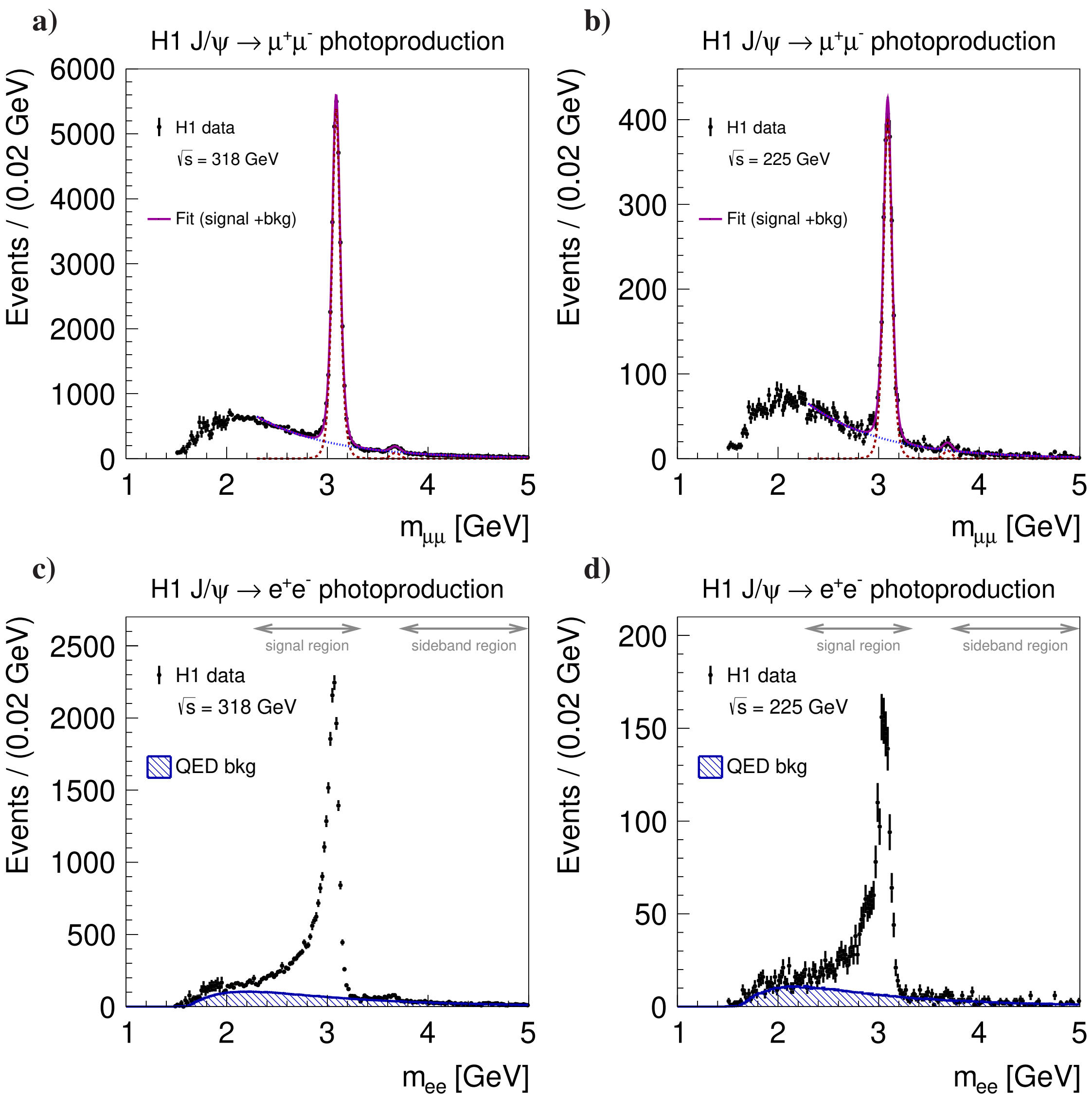

Figure 2: Di-lepton invariant mass distributions for the high- and low-energy data sets in the $J/\psi \to \mu^+\mu^-$ decay channel, figures a) and b), respectively, and for the $J/\psi \to e^+e^-$ decay channel, figures c) and d), respectively. For the muon sample the fits used to reconstruct the number of J/ψ mesons are shown as well. For the electron sample the simulation of the QED background $ep \to eX\ e^+e^-$ is given by the shaded region and the J/ψ signal and sideband normalisation regions are indicated.

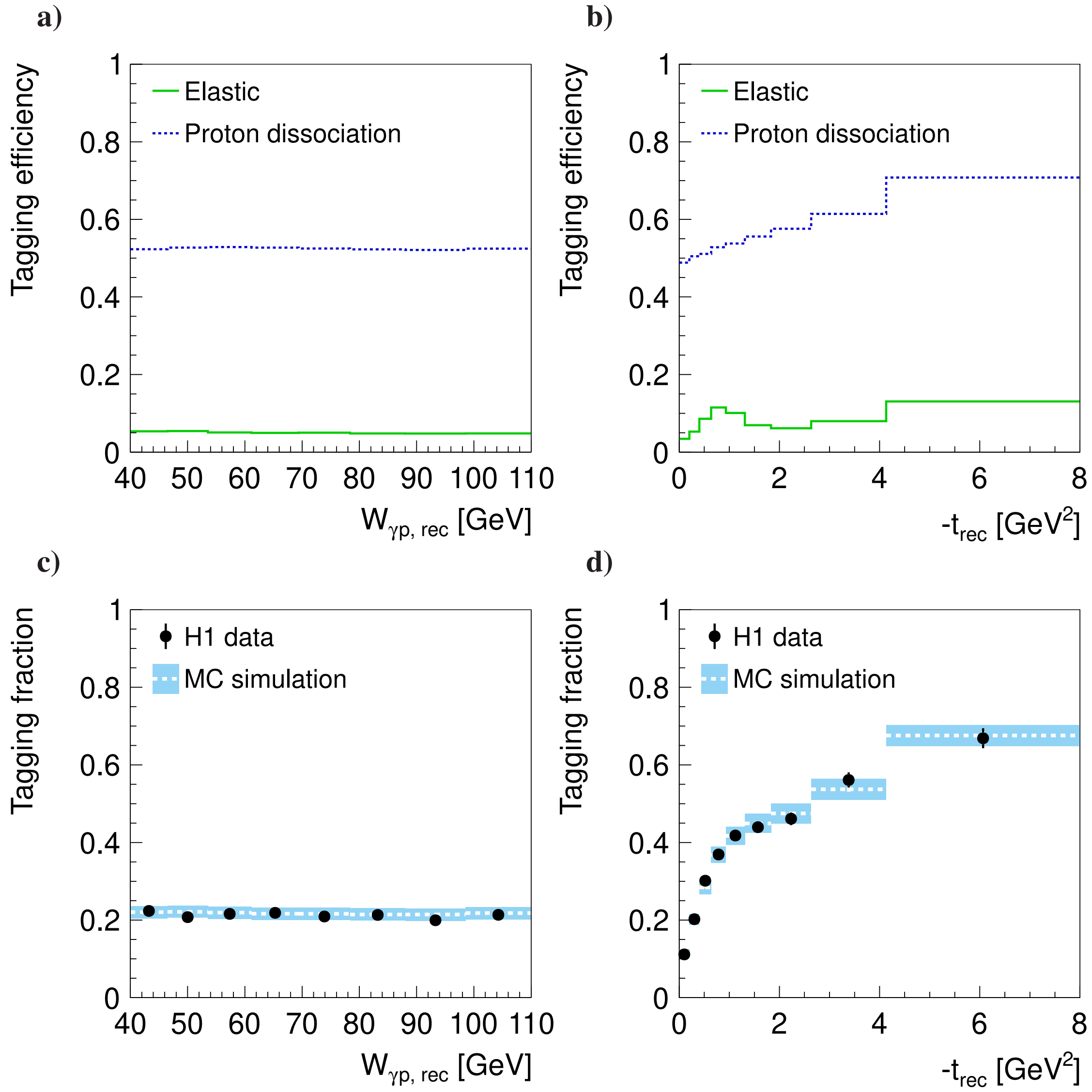

Figure 3: Tagging efficiencies as functions of (a) $W_{\gamma p,rec}$ and (b) $-t_{rec}$ as obtained from the simulations of elastic and proton-dissociative J/ψ production. Tagging fractions as functions of (c) $W_{\gamma p,rec}$ and (d) $-t_{rec}$, as obtained from the e^+e^- data set in the invariant mass window $m_{ee} = 2.3 - 3.3\,\mathrm{GeV}$. The data set contains elastic and proton-dissociative J/ψ decays, as well as $ep \to eX\ e^+e^-$ events. It is compared to the simulation based on the event generators DIFFVM and GRAPE. The data (simulations) are shown by points (shaded bands). The vertical spread of the bands represents the uncertainty due to the tagging in the simulation.

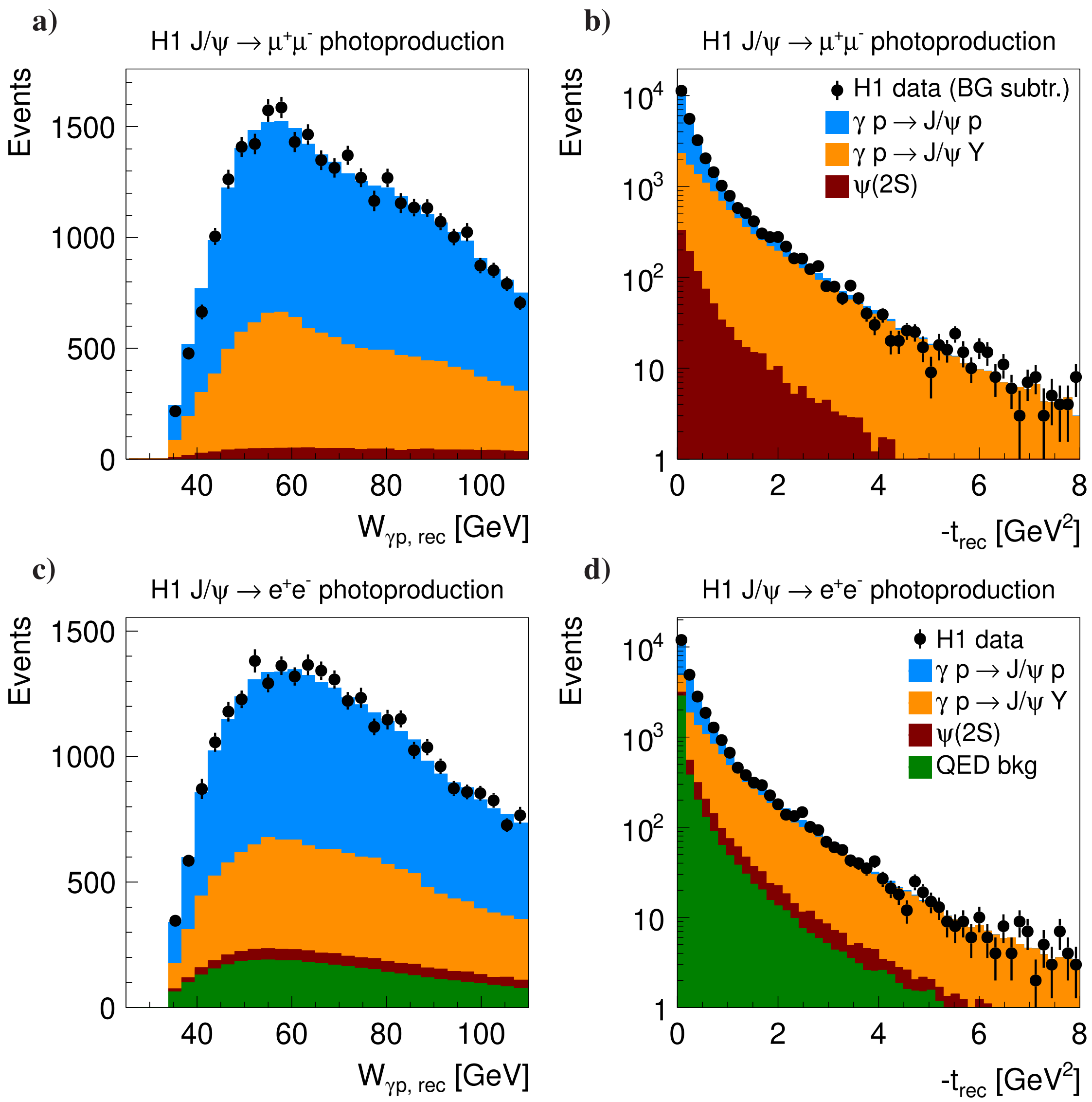

Figure 4: Observed distributions as functions of $W_{\gamma p,rec}$ and $-t_{rec}$ restricted in $m_{\ell\ell}$ to the J/ψ signal region. The muon sample is shown in a) and b), the electron sample is shown in c) and d). The data, shown by the points, are compared to the simulation of elastic and proton-dissociative J/ψ production. Also shown is the contribution from $\psi(2S)$ events and, for the electron sample only, the QED background. For the muon sample, background is subtracted from the data using a sideband method.

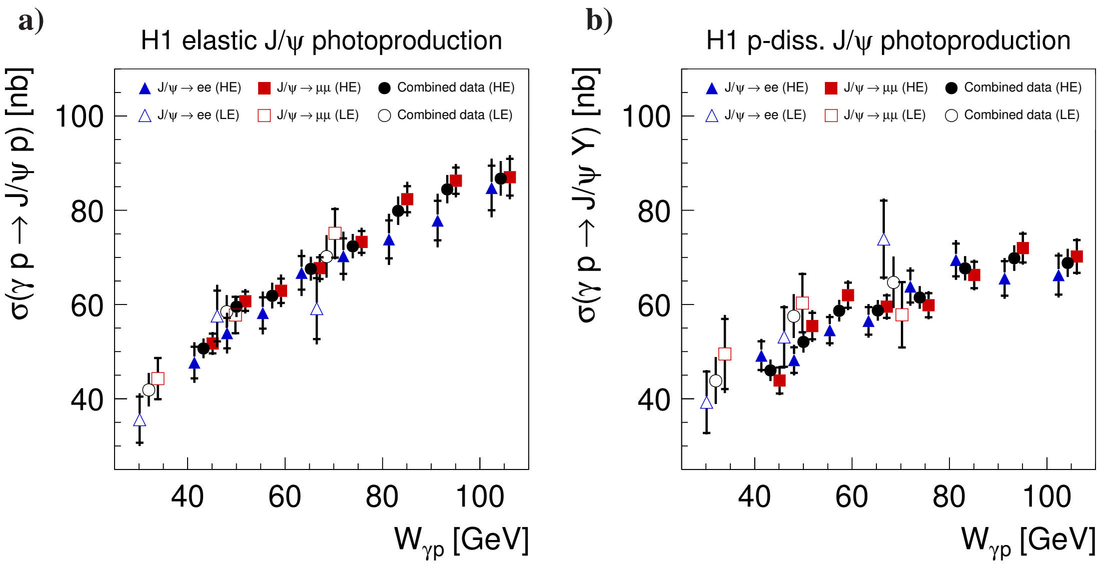

Figure 5: Combined elastic and proton-dissociative cross sections as a function of $W_{\gamma p}$ (circles) compared to the input data from $J/\psi \to e^+e^-$ (triangles) and $J/\psi \to \mu^+\mu^-$ (squares) of the HE and LE data sets. The error bars of the input data indicate the uncertainty composed of the statistical errors (inner error bars) and statistical errors combined with all individual systematic uncertainties (full error bars). The error bars of the combined data points reflect the uncertainty after the combination. The combined data points are drawn at their bin centres. The electron and muon data points are shifted in $W_{\gamma p}$ for better visibility.

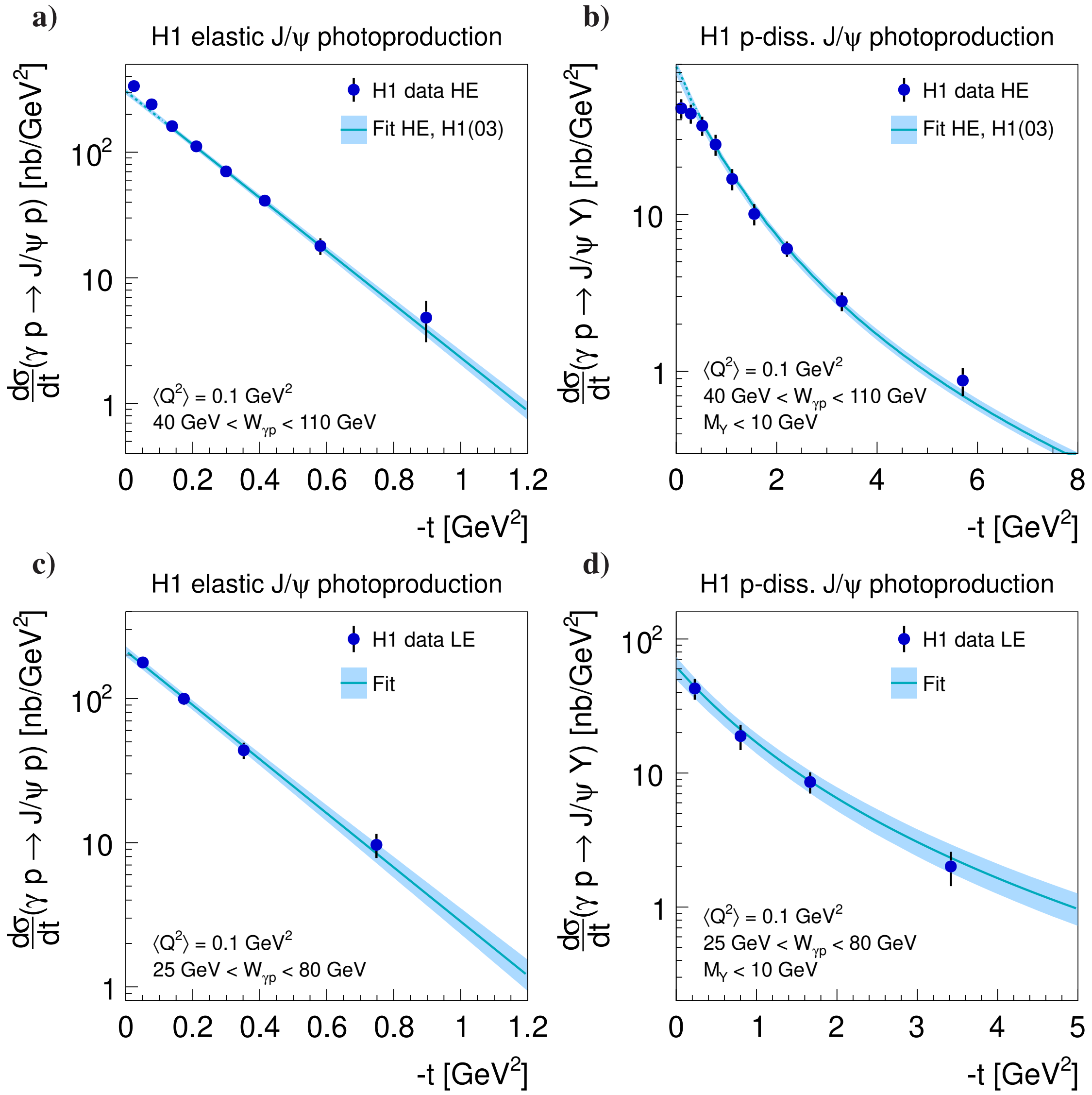

Figure 6: Differential J/ψ photoproduction cross sections $\mathrm{d}\sigma/\mathrm{d}t$ as a function of the negative squared four-momentum transfer at the proton vertex, $-t$, as obtained in the high-energy data set for the (a) elastic regime and the (b) proton-dissociative regime and as obtained for the low-energy data set shown in (c) and (d). The error bars represent the total errors. Also shown by the curves is a simultaneous fit to this measurement and [24] of the form $\mathrm{d}\sigma/\mathrm{d}t = N_{el}e^{-b_{el}|t|}$ for the elastic cross sections and $\mathrm{d}\sigma/\mathrm{d}t = N_{pd}(1 + (b_{pd}/n)|t|)^{-n}$ for the proton-dissociative cross sections. The fit uncertainty is represented by the spread of the shaded bands.

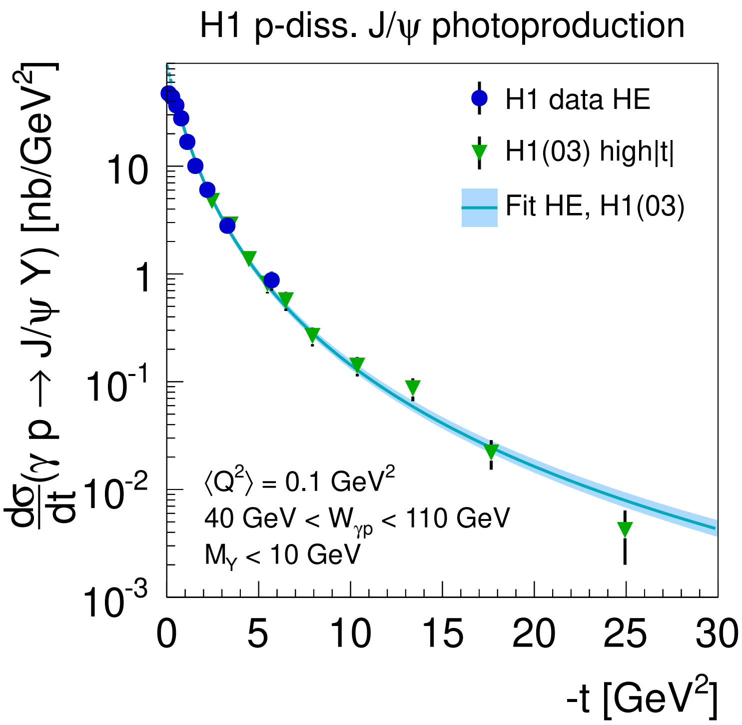

Figure 7: Proton-dissociative cross section as a function of $-t$ (full circles) compared to a previous measurement at high $|t|$ [24] (triangles) interpolated to match the $W_{\gamma p}$, Q^2 and M_Y ranges of the current measurement. The curve represents a simultaneous fit to both data sets, the spread of the shaded band its uncertainty.

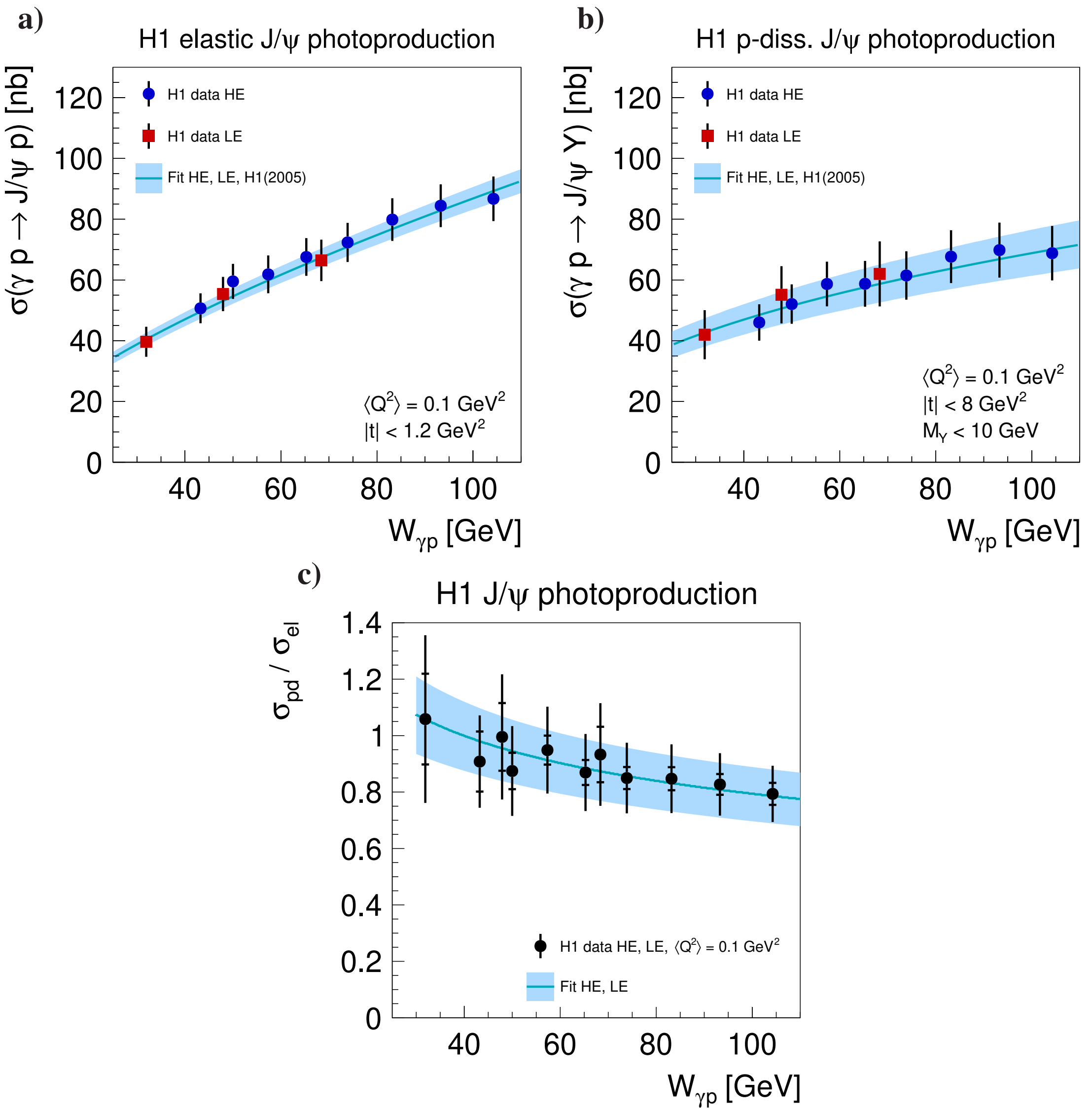

Figure 8: J/ψ photoproduction cross sections as a function of the photon proton centre-of-mass energy $W_{\gamma p}$ for (a) the elastic and (b) the proton-dissociative regime. The data from the high-energy data set are shown by circles, the data from the low-energy data set as squares. The error bars represent the total errors. Shown by the curves is the simultaneous fit to the data from this measurement and [4], see figure 9. The fit uncertainty is represented by the shaded bands. In (c) the ratio of the proton-dissociative to elastic J/ψ photoproduction cross section is shown. The data are presented as full circles and the vertical bars indicate the total uncertainties, including normalisation uncertainties. The inner error bars represent the bin-to-bin uncorrelated errors, determined in an approximative procedure. The curve is the ratio of the fits shown in (a) and (b). The shaded band indicates the uncertainty on the ratio obtained from the fit uncertainties.

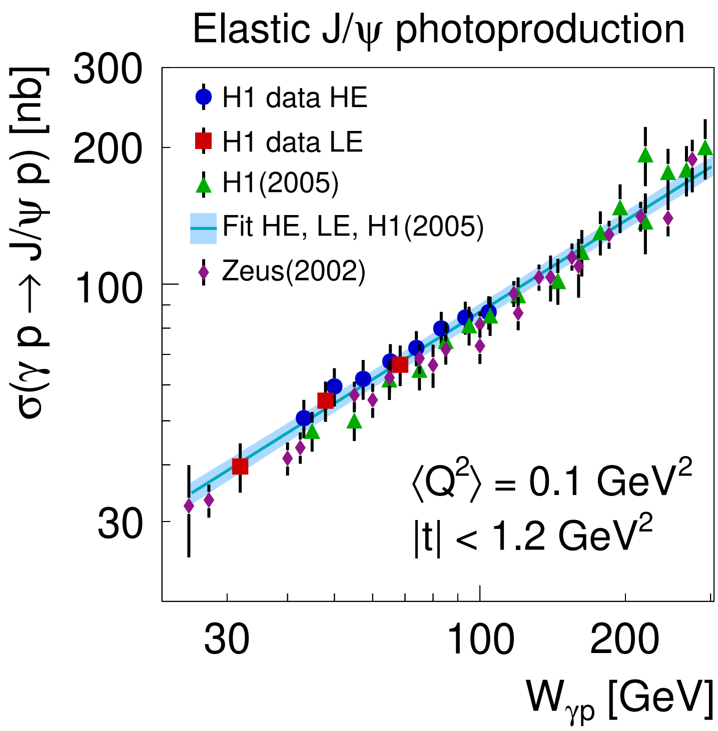

Figure 9: Elastic cross sections as a function of $W_{\gamma p}$ from this measurement compared to previous measurements at HERA [4, 5]. The shaded band represents a fit to the present data and [4] together with its uncertainties.

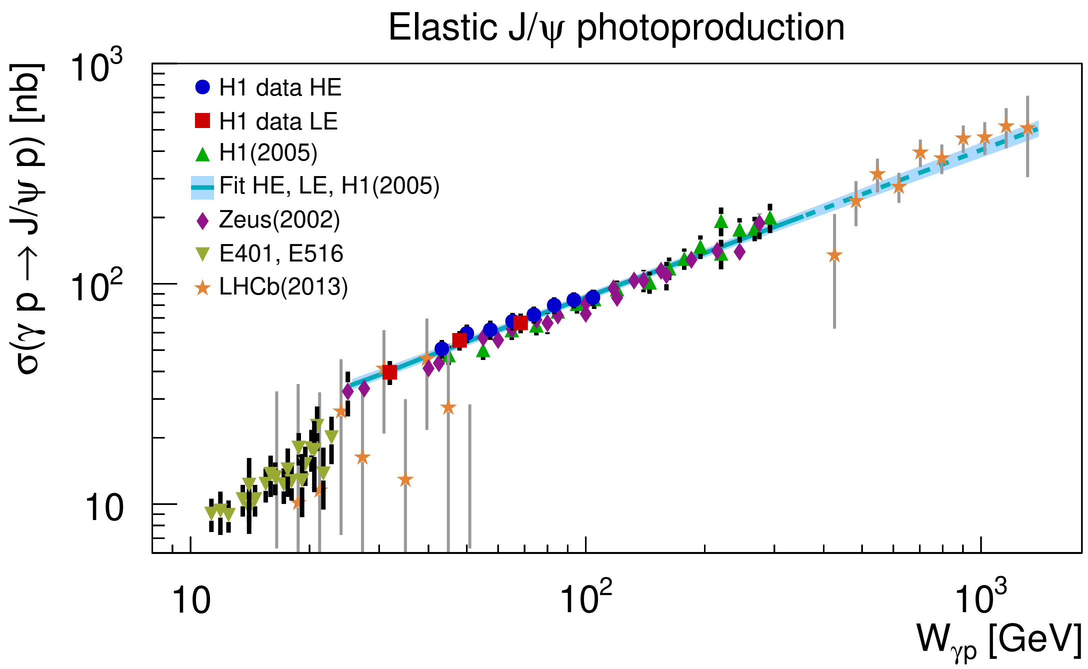

Figure 10: Compilation of elastic J/ψ production cross section measurements including this measurement, previous HERA results [4, 5], results from fixed target experiments [26, 27] and from LHCb [53]. Also presented is the fit to the H1 data only, indicated by the curve. The fit is extrapolated in $W_{\gamma p}$ from the range of the input data to higher values, as shown by the dashed curve. The shaded band indicates the uncertainty on the fit.

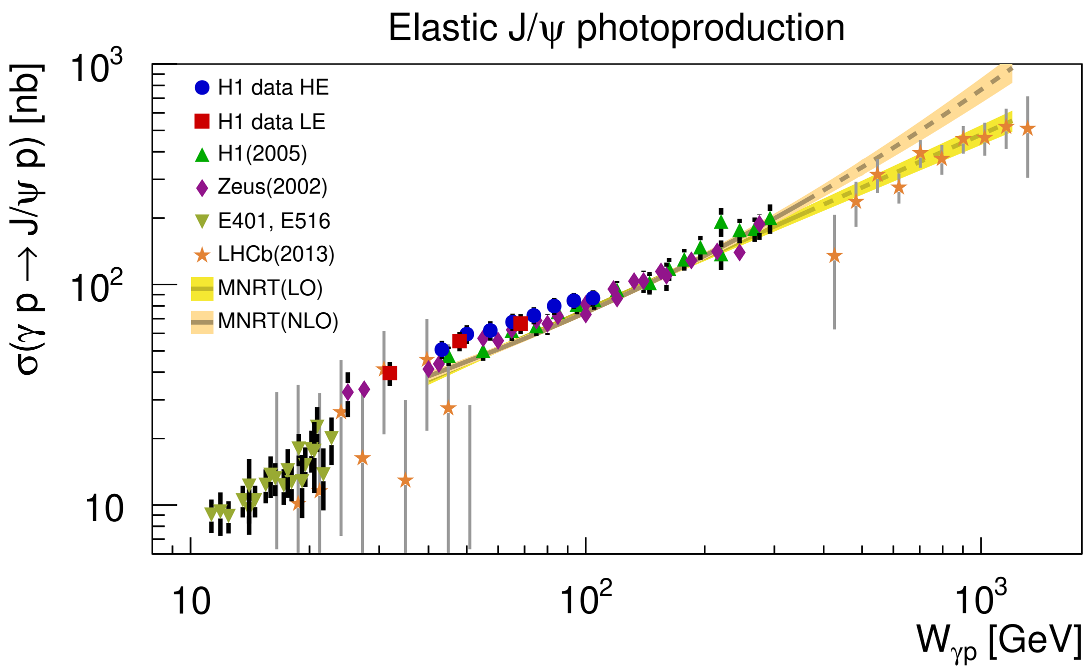

Figure 11: Compilation of elastic J/ψ production cross section measurements including this measurement, previous HERA results [4, 5], results from fixed target experiments [26, 27] and from LHCb [53]. Also presented are QCD fits from [14] to the previous HERA data [4, 21–23] to determine a gluon density at leading-order and next-to-leading order, indicated by the curves. The fits are extrapolated in $W_{\gamma p}$ from the range of the input data to higher values, as shown by the dashed curves. The shaded bands indicate the fit uncertainties.